Geophys. J. Int. (2007) **169,** 170–188 doi: 10.1111/j.1365-246X.2006.03287.x

Seismic anisotropy of the Slave craton, NW Canada, from joint interpretation of *SKS* and Rayleigh waves

David Snyder and Marianne Bruneton

Geological Survey of Canada, Natural Resources Canada, 615 *Booth Street, Ottawa, Ontario* K1A 0E9 *Canada. E-mail: dsnyder@NRCan.gc.ca*

Accepted 2006 November 1. Received 2006 November 1; in original form 2006 May 16

SUMMARY

Teleseismic events recorded at a 25-element array in NW Canada between 2001 and 2006 provided sufficient distribution in back azimuth to demonstrate birefringence in *SKS* and *SKKS* waves as well as directional dependence of Rayleigh-wave phase velocities. Typical delays between orthogonally polarized *SKS* waves are 0.8–1.2 s, and modelling of azimuthal dependence indicates two nearly horizontal layers of anisotropy within the mantle. Anisotropy of Rayleigh waves is generally consistent with models of layered *Vs* anisotropies that increase with depth from 1 per cent at the Moho to 9 per cent at 200 km but vary between subarrays. Consistency between the *SKS* and Rayleigh wave anisotropies in one subarray suggests that the assumption of symmetry about a horizontal axis is valid there but is not fully valid in other parts of the craton. The upper layer of anisotropy occupies approximately the uppermost 120 km in which the fast polarization direction strikes generally north–south, coinciding with regional-scale fold axes mapped at the surface. The fast polarization direction of the deeper layer aligns with current North America plate motion, but its correlation with trends of coeval kimberlite eruptions within the Lac de Gras field suggests it can be at least partly attributed to structural preferred orientation of vertical dykes inferred to exist to depths of 200 km.

Key words: continental lithosphere, polarization, Rayleigh waves, seismic anisotropy, shear wave splitting, Slave craton.

1 INTRODUCTION

Seismic anisotropy provides the best indicators of ordered structures, sometimes collectively called 'fabric', within subcontinental mantle lithosphere. These indicators complement the broader bulk physical properties mapped by tomography or the localized discontinuities revealed by forward scattering reconstructions or receiver functions. The Slave Array, 25 remote portable seismic observatories deployed within the Slave craton in the Northwest Territories of Canada between 2001 September and 2006 January, recorded earthquakes used for all of these analyses (Snyder *et al.* 2004). Here we describe only the azimuthal dependence of delay times (splitting) between orthogonal components of *SKS* and *SKKS* waves and of Rayleigh wave phase velocities. Both wave types display dependence on the backazimuth for each of the 58 earthquakes studied; the Rayleigh waves indicate some depth dependence of the azimuthal variation of fastest seismic velocity.

Because *SKS* splitting contrasts velocity components within horizontal planes, whereas Rayleigh waves travel in vertical planes and their phase velocities are most dependent on vertical velocity gradients, joint interpretation provides information about the 3-D velocity tensor and true (rather than assumed) axes of symmetry (Montagner *et al.* 2000; Li *et al.* 2003). Broadly consistent anisotropy estimates across the Slave Array suggest that the mantle lithosphere fabric, while not simple, is relatively coherent and varies gradually compared to many continental regions (Savage 1999). A number of recent studies characterized seismic anisotropy of mantle lithosphere using surface waves (e.g. Li *et al.* 2003; Gaherty 2004; Debayle *et al.* 2005), body waves (e.g. Schultze-Pelkum & Blackman 2003) or both (Brisbourne *et al.* 1999; Montagner *et al.* 2000). The Precambrian subcontinental mantle lithosphere of the Slave craton provides an especially attractive setting for such methodology comparisons because of its strong and layered anisotropic structure.

Active exploration for diamonds within the Slave craton over the past two decades resulted in an unusually rich petrological understanding of its mantle as derived from mantle xenoliths and xenocrysts found within the kimberlite eruptions (e.g. Griffin *et al.* 1999; Grütter *et al.* 1999; Kopylova & Caro 2004; Heaman *et al.* 2006). Recent surface mapping and related studies have similarly provided important constraints on the geological history of the craton (e.g. Bleeker *et al.* 1999; Davis *et al.* 2003). All of these results provide a context for interpretation of mantle layers with distinct seismic properties as underthrust and stacked lithosphere through which sheeted kimberlite eruptions brought diamonds to the near surface (Snyder & Lockhart 2005).

2 DATA AND METHODS

2.1 Shear wave (*SKS*) splitting

Observations of *SKS* splitting consist of three-component digital data recorded at 24 broad-band stations operated by the POLARIS

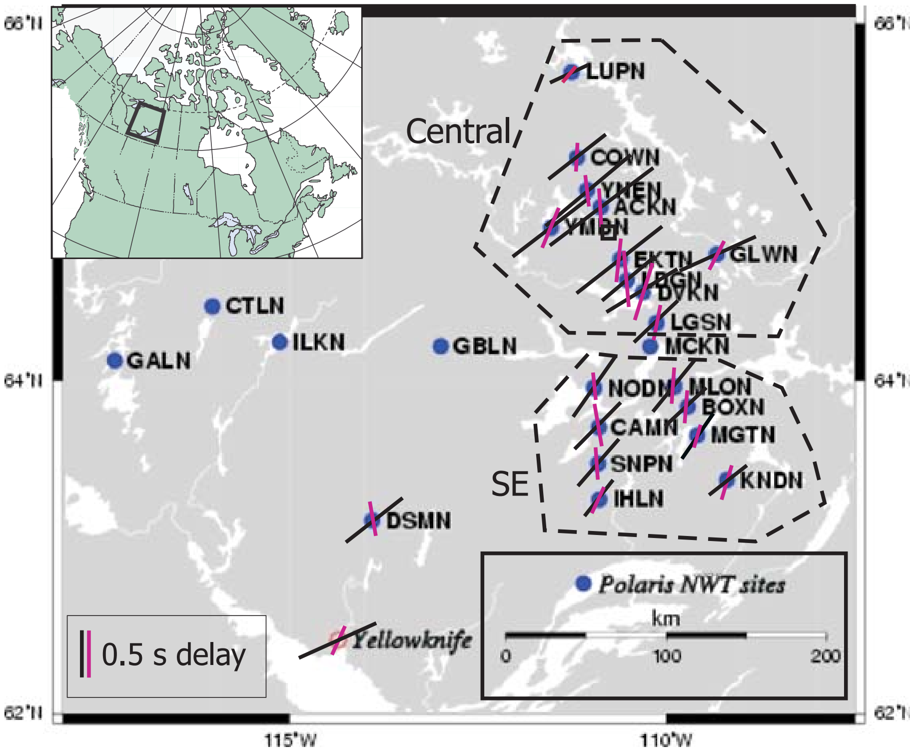

Figure 1. Location of the POLARIS Slave (NW Territories) array. Black and grey line segments indicate fast polarization and delay time of *SKS*/*SKKS* waves for two anisotropic layers as modelled using *SKS*/*SKKS* waves recorded at that station. Irregular dashed polygons group stations into subarrays used in Rayleigh wave studies; the remaining six stations in the west formed the Southwest array.

Table 1. Station locations.

Station	Latitude °N	Longitude °E	Elevation	Start	End	Code
EKTN	64.6985	−110.610	458 m Ekati airstrip[b]	14-Sep-01	14-Jul-06	E
ACKN	64.992	−110.871	469 m Achilles Lake	09-Sep-01	11-Jul-06	A
BOXN	63.852	−109.717	436 m Box Lake	02-Aug-02		B
CAMN	63.732	−110.899	420 m Camsell Lake	29-Jul-02	15-Jul-05	C
COWN	65.268	−111.186	513 m Contwyoyo Lake	19-Jul-02		W
DVKN	64.509	−110.310	420 m Diavik airstrip[b]	25-Jul-02	17-Jul-06	D
DSMN[a]	63.179	−113.900	307 m Discovery Mine site	18-Jul-03	23-Jul-05	V
GLWN	64.725	−109.330	449 m Glow worm Lake	23-Jul-02		G
IHLN	63.305	−110.891	417 m Indian Hill Lake	31-Jul-02	18-Jul-05	I
KNDN	63.419	−109.201	421 m Kennady Lake	04-Aug-02		K
LDGN	64.579	−110.522	416 m Lac de Gras N shore	13-Sep-01	3-May-06	L
LGSN[a]	64.334	−110.131	440 m Lac de Gras SW shore	24-Jul-02	17-Jul-06	Q
LUPN	65.738	−111.256	505 m Lupin Mine site[b]	11-Jul-03	22-Jul-06	U
MCKN	64.198	−110.213	431 m MacKay Lake N shore	26-Jul-02		M
MGTN	63.686	−109.591	411 m Margaret Lake	04-Aug-02	15-Sep-05	T
MLON	63.970	−109.895	418 m Marlo Lake	03-Aug-02		O
NODN	63.961	−110.960	435 m Nodinka Narrows	29-Jul-02	17-Jul-05	N
SNPN	63.518	−110.908	458 m S of Snap Lake	31-Jul-02		S
YMBN	64.874	−111.533	439 m Yamba Lake	15-Jul-01	10-Jul-06	Y
YNEN[a]	65.088	−111.050	463 m NE of Yamba Lake	24-Jul-02	9-Jul-06	X
CTLN	64.6985	−110.6097	468 m Castor Lake	18-Jul-04		P
GALN	64.1167	−117.3142	340 m Gameti airstrip	20-Jul-04		R
GBLN	64.1995	−112.9935	392m Grizzle Bear Lake	24-Sep-03		Z
ILKN	64.2241	−115.1293	Xxx m Indin Lake	27-Sep-03		J

[a]CMG-40T seismometer. [b]AC power.

consortium (Fig. 1, Table 1; www.polarisnet.ca) and at the multi-element Yellowknife seismic observatory (station YKW, e.g. Bostock 1998). The POLARIS Slave array was designed as primarily a linear (2-D) array with a few outlier stations for some 3-D control. The linear array was oriented to be perpendicular to known major geochemical trends in the mantle (Grütter *et al.* 1999) and to maximize earthquake sources in the southwest Pacific and in South America along the great circle that includes the profile. Stations were equipped with Guralp CMG-3ESP (100 s corner period) or CMG-40T (30 s corner period) seismometers (Table 1), Nanometrics Trident digitizers and Libra satellite telemetry, most powered by solar panels. Only a few stations (DVKN, EKTN and LUPN) located at gold or diamond mines operated on AC power throughout the Canadian winter. These stations variously recorded up to 58 earthquakes (Table 2) of magnitude M_b 5.8–8.7 with an epicentral distance between 88° and 118°. The Slave array is so located that earthquakes with epicentral distances appropriate for *SKS* and *SKKS* splitting are located at a large number of backazimuths (Tables 2 and 3); in this study nearly continuous coverage occurs between azimuths of 237° and 336°.

Seismograms with clear and distinct *SKS* or *SKKS* arrivals were consistently bandpass filtered with a 0.02–0.5 Hz Butterworth filter in order to remove frequency dependence of the splitting parametrization. Splitting parameters for individual events were estimated in two ways using the grid search method of Silver & Chan (1991) (Fig. 2), first by minimizing the energy on the transverse component, second by maximizing eigenvectors that indicate linear particle motion. Low uncertainties as well as consistency between the two estimates of the delay time (δt) between the fastest and slowest components and the polarization angle of the fast shear wave (ϕ) indicated reliable estimates (also see Özalaybey & Savage 1994; Silver & Savage 1994). The analysis window was varied to maximize the consistency. The resulting estimates of δt and ϕ for each station-azimuth (Fig. 3, Table 3) are the average of the two types of estimates using all earthquakes recorded at that station within that backazimuth bin over the five years studied. Each bin is 2–3 degrees wide. The splitting parameters for each backazimuth were thus based on two to seven earthquakes; greater numbers of earthquakes decrease uncertainty in the estimates at each azimuth as represented by the standard deviations shown in Fig. 3 and listed in the last rows of Table 3.

2.2 Rayleigh wave studies

The data for Rayleigh surface wave studies consist of the vertical component of digital data recorded at the same stations as for the *SKS* analysis plus four stations in the western Slave craton (Fig. 1). We selected earthquakes of magnitude greater than 5.5 that exhibit a good quality Rayleigh wave signal whilst trying to keep an even azimuthal distribution (Fig. 4). Preprocessing included correcting for the instrument response (Darbyshire & Asudeh 2006) and extraction of the fundamental-mode Rayleigh wave from the vertical component of the record using a phase-matched filter (Herrin & Goforth 1977; Lander & Levshin 1989). Using the array method of Pedersen *et al.* (2003, Pedersen *et al.* 2006), the average Rayleigh-wave phase velocity and its azimuthal variations were calculated by a three-step analysis: (1) determining the backazimuth of each incoming surface wave and its mean phase velocity across the array, (2) calculating the overall mean phase velocity and (3) retrieving the azimuthal variation of the phase velocity.

This first part of the analysis effectively consisted of determining the plane wave that best fits the Rayleigh wave observed at each frequency. For each event k and station pair (i, j), the time delays $\Delta t_{ij}^k(f)$ were measured as a function of frequency. Time delays are proportional to the phase of the Wiener filter of the two signals (Wiener 1949; Hwang & Mitchell 1986). The Wiener filter is the ratio of the cross-spectrum of the two signals to the autospectrum of a reference signal taken as one of the two signals plus a constant. The cross- and autospectrum are apodized by applying a Hanning window in the time domain, which has the advantage of objectively reducing incoherent noise. The constant is used as an energy threshold to stabilize the measurement; here we preferred keeping the constant at zero and rejecting all measurements with a coherence lower than 0.95.

The time delays $\Delta t_{ij}^k(f)$ were then inverted for each event k to obtain the best slowness vector for that event. As it is important to minimize the influence of outliers, the misfit $F_1^k(f)$ was estimated as the mean absolute difference (L1 norm) between the observed and estimated delays. This inversion yielded $\theta^k(f)$ and $C^k(f)$, respectively the backazimuth and phase-velocity associated with the best-fitting slowness vector. The observed backazimuths $\theta^k(f)$ differ generally less than 5° from the great circle path, with a maximum discrepancy of 13°. Most events from a particular region deviate with the same trend. For the following steps we rejected $\theta^k(f)$ and $C^k(f)$ measurements with a misfit $F_1^k(f)$ larger than a threshold because a large misfit indicates that a plane wave is not a good solution to the delay measurements of event k at frequency f due, for example, to contamination by noise or diffraction effects. The threshold was empirically set to 4 s.

In the second step, $C(f)$ was determined as the inverse of the slope of the best-fitting line through all ($\Delta t_{ij}^k(f)$, $D_{ij}^k(f)$) points. The distances $D_{ij}^k(f)$ are the interstation distances projected onto backazimuth $\theta^k(f)$. We required that the line go through the origin, and we used the L1 norm for misfit estimation $F_2(f)$. To obtain an accurate estimate we first fit a straight line to all available points, then rejected ($\Delta t_{ij}^k(f)$, $D_{ij}^k(f)$) points with a misfit (in this last inversion) larger than twice the mean absolute misfit and then re-estimated the phase-velocity $C(f)$ and mean misfit $F_2(f)$ on the reduced data set. Following Pedersen *et al.* (2003), the uncertainty on the phase velocity is estimated as $C_{\max}(f) - C(f)$ where

$$C_{\max}(f) = \frac{D_{\max}(f)}{D_{\max}(f)/C(f) - F_2(f)}, \tag{1}$$

where $D_{\max}(f)$ is the maximum value of $D_{ij}^k(f)$. The uncertainty thus obtained is larger when the interstation distances are shorter, and corresponds fairly closely to the standard deviation of all $C^k(f)$ curves in the case where the number of stations available is the same for all events.

In the presence of azimuthal anisotropy, dependence of surface wave phase velocity on the azimuth can be written (e.g. Babuška & Cara 1991) as

$$\begin{aligned} C_{th}(f) = C_0(f)[1 &+ A_1\cos(2\theta) + A_2\sin(2\theta) \\ &+ A_3\cos(4\theta) + A_4\sin(4\theta)], \end{aligned} \tag{2}$$

where $C_{th}(f)$ denotes the theoretical phase-velocity of a surface wave in an azimuthally anisotropic medium. $C_0(f)$ is the average phase-velocity and $A_1 - A_4$ are constants that are structure and frequency dependent. The procedures used subsequently to find the best-fitting velocity $C_{th}(f)$ showed that the 2θ terms were dominant, in accordance with most other studies of Rayleigh wave fundamental-mode phase velocity variations. The previous equation can then be rearranged into

$$C_{th}(f) = C_0(f)\left\{1 + \frac{A(f)}{2}\cos[2(\theta - \theta_0)]\right\}, \tag{3}$$

which has more direct physical meaning because it gives the fast direction as θ_0, and the apparent peak-to-peak percentage of anisotropy as $A(f)$.

Finally, in order to analyse the azimuthal variation of the Rayleigh-wave phase velocity, we applied the same array analysis described previously on subsets of events having backazimuths

Table 2. Earthquakes used for SKS anisotropy studies at the POLARIS Slave Array.

Event	Δ (deg)	BAz (deg)	ϕ (deg)	Dt (s)	Stations	Earthquake location
13sep02 22:28	100	336	32	0.73	ABCWDIKLQONS	India
8sep02 18:44	100	284	24	1.95	Not GMYUV	Papua N. Guinea
10oct02 10:50	102	292	31	1.35	ABCWGTONSY	Papua N. Guinea
11mar03 07:27:32	97	274	36	1.63	CDEIQMSY	Papua N. Guinea
31mar03 01:06	100	275	38	1.33	BCTOSY	Papua N. Guinea
27apr03 16:03	104	252	20	1.08	Not AGKLNXUV	Vanuatu
13may03 21:21	102	256	22	1.00	BCWDEQTOSY	Vanuatu
26may03 19:23	102	300	35	1.93	BCWDEOSY	Halmahera
7jun03 00:32	98	275	31	1.05	BCWDQTOSY	Papua N. Guinea
12jun03 08:59	97	271	28	1.43	BCWEQTOSY	Papua N. Guinea
28jun03 15:29	99	281	32	1.65	BCWDETOSY	Papua N. Guinea
21jul03 13:53	99	277	27	1.53	ABCWDGILNSYX	Papua N. Guinea
22jul03 04:21	101	257	18	1.18	Not EMV	Vanuatu
25jul03 09:37	95	278	34	1.43	Not MUV	Papua N. Guinea
27jul03 11:41	92	137	9	0.80	Not DMUV	Bolivia
11aug03 21:22	101	336	42	0.68	Not WDEG	India
25jan04 11:43:12	95	239	33	0.43	ABCDILNSYXU	Tonga
5feb04 21:05:01	103	290	31	1.93	Not WMT	Irian Jaya
7feb04 02:42:35	103	290	31	1.73	Not WGMT	Irian Jaya
8feb04 08:58:49	103	290	41	1.68	ABCDEILONX	Irian Jaya
17mar04 03:21:07	93	138	21	1.08	BWDEGLQOSYXV	Bolivia
23apr04 01:50:30	113	300	36	2.08	Not T	Savu Sea
25apr04 02:19:21	105	251	37	1.15	Not ELMT	Loyalty Islands
27apr04 23:28:21	102	254	26	0.80	Not LMT	Vanuatu
3may04 04:36:51	107	149	28	0.85	Not MT	Chile
30jun04 23:37:25	103	301	37	1.70	Not QMTNX	Sulawesi
15jul04 04:27:10	97	243	9	0.62	Not QMTN	Fiji
25jul04 19:28	112	322	37	0.65	Not TN	Sumatra
28jul04 03:56:28	101	293	33	1.63	Not QTN	Indonesia
28aug04 13:41:29	104	147	24	1.05	ABWGKMONYXUV	Argentina
7sep04 11:53:06	100	140	4	0.50	Not YXUV	Argentina
8oct04 08:27:54	98	262	18	1.30	Not MX	Solomon Is.
9nov04 23:58:23	98	261	15	1.12	Not M	Solomon Is.
16nov04 10:06:53	98	274	36	1.15	ABWDGQNSYV	New Britain
26nov04 02:25:06	103	290	31	1.93	Not MTS	Papua N. Guinea
1jan05 06:25:44	108	335	28	0.70	CKLONUV	N. Sumatra
5feb05 12:23:15	99	306	37	2.08	Not ABCWMV	Celebes Sea
26feb05 12:56:52	111	331	23	1.05	Not WQM	Indonesia
2mar05 10:42:05	109	294	36	1.65	Not WMO	Banda Sea
21mar05 12:23:52	96	137	5	0.55	Not M	Salta, Argentina
28mar05 16:09:37	111	330	52	1.18	Not M	N. Sumatra
10apr05 10:29:13	114	327	15	0.60	Not LM	Indonesia
11apr05 12:20:05	99	280	37	1.33	Not BCLM	Papua N. Guinea
11apr05 17:08:54	105	250	6	1.23	Not LM	SE Loyalty Is.
16apr05 16:38:06	111	330	4	1.08	Not LM	Nias, Sumatra
10may05 01:09:07	118	321	32	0.53	Not LQMTONSV	Sumatra
14may05 05:05: 81	112	328	−3	0.50	Not M	Nias, Sumatra
16may05 03:54:11	110	237	81	0.83	Not LQMTX	Kermadec
19may05 01:54:53	111	330	14	0.73	Not WDLM	Indonesia
4jun05 14:50:48	101	278	33	1.38	Not MX	Papua N. Guinea
5jul05 01:52:04	111	330	−5	0.83	BCWDEGILTONSYUV	Nias, Sumatra
24jul05 15:42:05	105	336	39	0.93	ABWDEGKLQMTOSY	Nicobar Is.
26aug05 18:16:33	100	016	32	1.25	ABWEGLMTOSXU	Gulf of Aden
18sep05 07:26:00	88	336	24	1.85	ABWGKLQOSYU	Myanmar
25sep05 12:55:47	102	254	41	0.90	ABWGQMOSYU	Vanuatu
29sep05 15:50:26	98	274	18	1.45	AWDEQMOSU	Papua N. Guinea
19nov05 14:10:15	110	330	23	0.88	ABWEGKMO	Indonesia
11dec05 14:20:44	99	274	23	0.88	AEMOXU	Papua N. Guinea

Event is the date and time (hr:min:s) of the earthquake. Δ is the distance in degrees between EKTN and the earthquake; BAz is the backazimuth to the earthquake from EKTN. ϕ is the fast apparent anisotropy direction (in °); dt is the delay or splitting time (in s) as measured at EKTN or a nearby station. For station codes see Table 1.

Table 3. Measured splitting parameters as a function of backazimuths.

Station	16°	45°	137°	140°	148°	149°	237°	243°	250°	252°	254°	256°	257°	261°	271°	274°	276°	278°	280°	285°	290°	293°	294°	300°	301°	306°	321°	322°	327°	328°	330°	336°	Station
LUPN	49	36	37		−26		37	6	33		36		6	52	−23	66	61	44	40		41	39	47	57	53	45	62	66	70	−28	79	45	LUPN
	0.68	1.27	0.60		0.68		1.28	0.35	0.35		0.73		0.52	0.45	3.00	0.5	1.00	0.53	0.85		0.95	0.8	0.68	0.58	0.7	0.88	1.20	1.33	1.55	2.15	0.3	0.62	
COWN	62		9	10	18	27	64	21	32	17	17	18	15	24	41	44	28	41	31	31	29	37		36	40		−23	−21	−27	−30	−25	28	COWN
	0.80		0.45	0.47	0.53	0.98	1.90	0.47	1.43	0.88	1.12	0.80	0.88	0.85	0.75	0.80	1.08	1.05	1.44	1.39	1.35	1.31		1.15	1.08		1.18	0.25	1.75	2.25	3.45	0.38	
YNEN	38	22	37		50	6	−6	31	17	34	38		34	33		32	44	32	34	31	39	34	42	40	63	40	−26	−23	13	−21	−5	54	YNEN
	1.35	0.82	0.43		0.80	0.68	0.88	0.68	0.88	0.90	1.63		0.82	0.78			1.05	1.25	1.58	1.48	1.80	1.95	1.46	1.85	1.95	2.23	1.20	0.28	0.30	1.52	0.35	0.65	
ACKN	39	19	22	28	23	17	26	21	25	28	28		22	29		39	26	34	29	26	33	33	40	39	38		−27	−2	−25	−12	13	28	ACKN
	1.23	1.62	0.45	0.75	0.80	0.88	0.65	0.78	1.20	0.95	1.05		1.10	1.05		1.3	1.48	1.25	1.98	1.53	1.65	1.68	1.55	1.88	1.70		0.95	0.47	1.42	0.88	0.61	0.57	
YMBN	34	−18	13		21	25	21	−6	24	23	29	22	26	27	36	43	38	40	37		34	42	39	38	42	40	−25	21	15	−12	7	44	YMBN
	1.53	0.95	0.64		0.70	0.73	1.33	1.13	1.02	0.98	1.05	0.98	1.08	1.10	1.05	1.25	1.25	1.16	1.33		2.38	1.25	1.65	1.58	1.73	2.23	1.05	0.43	0.60	1.05	1.05	0.73	
EKTN	25	1	6		25	28	27	30	26	20	26	15	16	18	28	18	27	31	32	27	32	33	36	37	37	37	−10	43		12	27	33	EKTN
	1.53	0.80	0.65		0.75	0.85	0.65	0.78	0.90	1.08		1.10	1.20	1.05	1.43	1.45	1.40	1.38	1.65	1.75	1.73	1.90	1.65	2.03	1.38	2.08	0.40	0.65		0.68	0.68	0.78	
GLWN	83	35	19	2	26	16	8	6	24	48	31		34	42		40	40	37	41		43	40	37	37	45	44	−27	−33	60	−39	−25	−13	GLWN
	0.57	2.08	0.85	0.60	0.82	0.70	1.58	0.25	1.10	2.12	2.37		0.81	0.85		1.08	0.88	0.80	0.82		1.10	0.85	0.95	1.23	1.00	0.35	1.15	1.85	1.33	2.70	2.92	0.90	
LDGN	45		7	−3	−29	−3	38	8	62				15	14		25	27	33		27	34	31	40		37	38		−7		−3	−1	43	LDGN
	0.78		0.73	0.53	4.00	0.63	0.55	0.60	0.65				1.23	1.02		0.88	1.53	1.30		1.68	1.55	2.02	1.83		1.77	2.30		0.53		0.50	0.75	0.65	
DVKN		8	−3	−9	−19	18	34	0	15	12	20	10	14	17		37	27	33	27	26	32	32	31	32	28		32	30		6	−5	29	DVKN
		0.50	0.75	0.78	3.25	0.65	0.35	0.55	1.18	1.00	0.65	1.00	1.15	0.95		1.13	1.60	1.38	1.60	1.25	1.20	1.88	1.05	0.35	1.93		0.53	0.65		0.43	0.82	0.73	
LGSN		32	13	12			58	21	79	15	17	9	7	76	22	36	54	30	41	33	20	26	19	29		12	34	39	3	−22	56	28	LGSN
		1.58	0.45	0.85			4.00	0.25	2.78	0.48	0.85	0.73	0.75	0.95	0.98	1.15	1.23	0.70	0.45	1.38	2.00	3.27	1.08	4.00		0.28	2.70	0.65	0.47	0.60	0.55	0.63	
MLON	62	−2	18	25	19	16	−11	−14	−2	16	18	4	3	14	28	37	9	26	22	26	32	32	34	31	36	−43	−29	−11	46	−2	−14	9	MLON
	0.43	1.10	.58	1.55	1.05	0.90	0.98	0.93	0.85	0.65	0.75	0.83	1.03	1.08	0.80	0.78	2.15	0.98	1.28	1.73	1.75	1.65	0.73	1.83	1.83	0.43	0.78	0.53	0.50	0.43	0.62	0.55	
BOXN			16	29	31	36	−20	−12	−4	6	39	4	10	16	40	53	29	28	26	32	30	28	27	33	35		−9	3	11	−15	1	11	BOXN
			1.08	1.25	0.68	1.33	0.68	0.88	1.30	0.68	1.03	1.00	0.73	1.10	1.03	1.25	1.33	1.03	1.14	1.00	0.90	2.23	0.88	2.00	3.08		0.33	0.46	0.47	0.88	1.12	0.53	
MGTN			31	−30			−35		27	28		19	21	16	26	28		31	33	24	26	34	26			28	−32		−2	−4	0	8	MGTN
			0.80	2.79			1.98		0.57	0.65		0.68	0.63	1.00	0.90	1.00		0.95	1.53	1.83	4.00	1.43	0.98			0.28	1.40		0.55	0.57	0.57	0.88	
KNDN	29	15	55	66		4	58	8	42	18	39		33	19			44	40	85	27	38	36	−67	37	37	30	30	−7	17	29	18	36	KNDN
	1.00	0.85	0.55	3.60		0.48	1.30	0.40	0.73	0.45	0.53		0.62	0.70			0.80	0.63	1.48	1.78	2.10	1.30	1.25	1.25	2.20	0.70	0.35	0.53	0.65	0.55	0.73	0.75	
NODN			−12	−29	9	−6	−11		17	14	22		15	20		30	18	29		23	43	29	48	−55		−3	57		−3	15	15	16	NODN
			0.65	2.15	0.65	0.85	0.83		1.05	1.53	1.18		1.18	1.08		1.23	1.38	1.20		2.15	1.58	2.90	1.50	1.28		0.17	4.00		0.53	0.53	0.78	1.00	
CAMN			−19	−17		9	67	14	3	10	13	12	12	11	29	31	21	28	22	24	31	28	41	−53	11		−1	−4	−7	−1	0	39	CAMN
			0.68	1.65		0.73	2.70	0.48	0.75	0.88	0.62	0.88	0.93	1.13	1.10	1.35	1.20	1.43	1.33	1.77	1.62	1.70	1.40	0.93	3.38		0.62	0.53	0.88	0.75	0.73	0.48	
SNPN		40	31	−29	−28	−2	66	68	5	17	9	13	15	11	24	25	29	29	29	28	32	34	43	35	38	−25		−10	−10	−10	1	26	SNPN
		1.18	0.47	2.17	3.65	0.80	2.95	0.43	0.80	0.65	1.53	0.85	0.78	1.18	0.95	0.98	1.00	1.03	1.03	1.23	1.78	1.88	1.27	2.58	1.88	0.30		0.73	0.75	0.75	0.70	0.72	
IHLN			−1	50	52	54	55	−19	−17	24	43		5	18		22	−17	26	51	32	38	32	36	34	35	19	−19	−16	−7	−8	15	8	IHLN
			0.23	3.90	3.30	2.28	3.38	0.88	1.40	0.58	0.63		0.73	0.65		0.80	1.83	0.68	1.00	0.68	1.10	0.93	0.85	1.30	1.98	0.28	0.40	0.53	0.78	0.50	0.43	0.73	
DSMN			−4	−3	46	22	69	−20	1	18	3			30		26	62		33	17	39	30	31	31	29		−35	−19	−12	−3	15	15	DSMN
			0.30	0.53	1.20	0.70	3.35	0.75	1.05	1.52				0.75		0.70	1.02	2.10	0.78		1.05	1.20	1.25	1.45	1.50		2.17	0.38	0.57	0.57	0.85	0.63	
YKW3			55	−42	50			66		48		61		45	46	46			46	29	46	50	38	43				45	51		51		YKW3
			0.75	4.00	1.85			1.75		0.65		0.65		0.85	0.65	0.80			0.80	1.20	1.45	1.10	1.85	1.90				2.00	2.35		0.35		
$\phi \pm$			13	2	7	5	10	10	20	24	19	5	15	12	1	12	7	5	9	7	10	6	5	2	5		13	15	7	7	18	19	
dt±			.11	.02	.09	.08	.12	.44	.20	.12	.19	.07	.08	.07	.02	.32	.17	.26	.17	.32	.58	.30	.44	.13	.47		.04	.09	.12	.12	.62	.09	

For each station, the top row is the fast apparent polarization direction in degrees, the second row is delay in seconds. The last two rows indicate typical uncertainties (standard deviations) in parameters at that backazimuth.

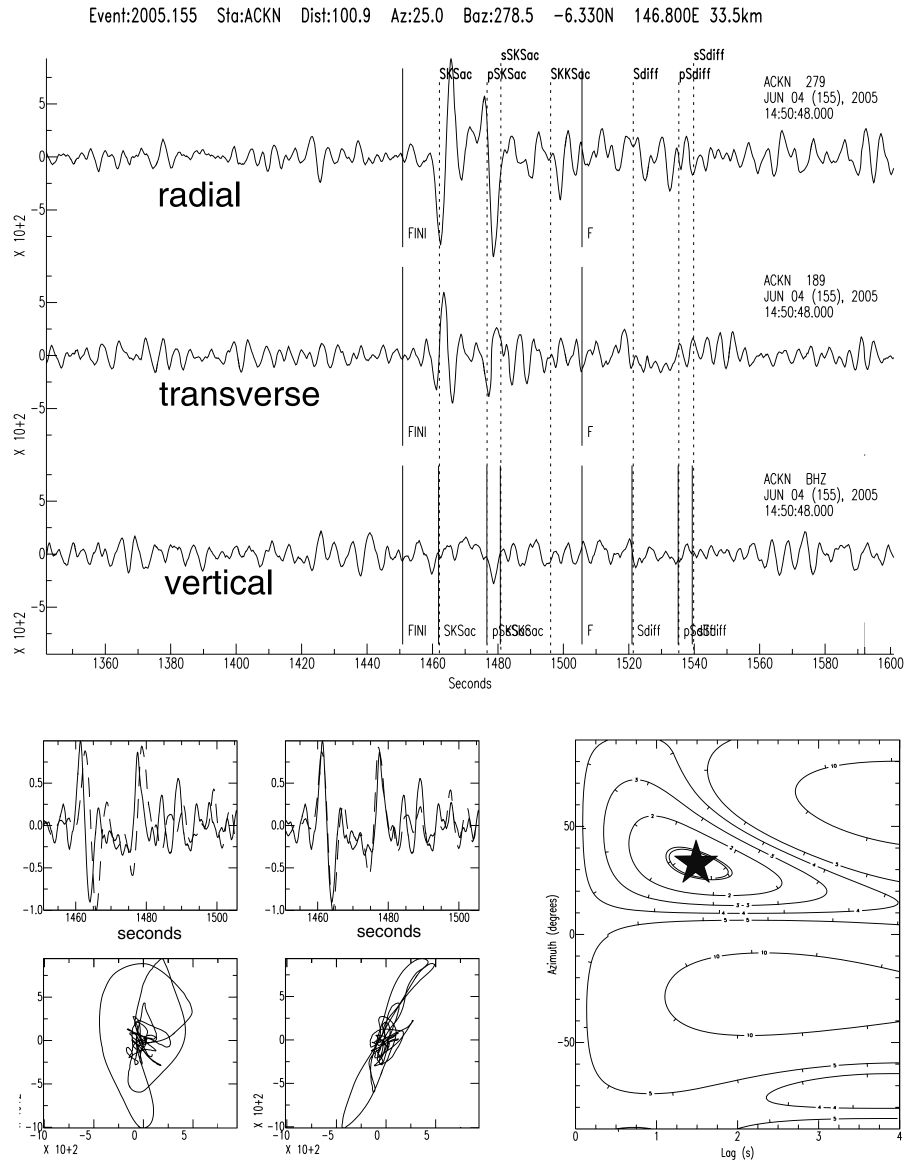

Figure 2. Three examples of *SKS* splitting analysis. Each example contains: (top) seismic traces resolved as radial, transverse and vertical components showing phase arrivals predicted from IASPEI 91 tables, FIN and F define the analysis window; (four diagrams in lower left) superposition of fast (ϕ) and slow ($\phi + 90$, dashed line) shear waves, uncorrected and corrected using the best estimate of ϕ and delay or lag δt, each above the corresponding plot of particle motion; (lower right) contour plot of the energy on the corrected transverse component showing minimum value (star) and 95 per cent confidence region (double contour). (a) M 6.1 earthquake in Papua New Guinea recorded at ACKN at $\Delta = 101°$ using both *SKS* and *SKKS* in this typical analysis. A fast polarization of 032 ± 4° and delay time of 1.50 ± 0.20 s were determined in this analysis. (b) M 6.7 earthquake in Indonesia recorded at KNDN at $\Delta = 115°$ in which analysis using *SKKS* illustrates a minimum in lag δt with respect to backazimuth. A fast polarization of 012 ± 18° and delay time of 0.65 ± 0.90 s were determined in this analysis. (c) M 6.8 earthquake in the Loyalty Islands recorded at LUPN at $\Delta = 105°$ using both *SKS* and *SKKS*. A fast polarization of 003 ± 23° and delay time of 0.50 ± 0.95 s were determined in this analysis.

within 20° wide bins. A 10° overlap between neighbouring bins makes every second one independent. Because the cosine function in the governing equations is symmetric, events coming from opposite directions were grouped into the same backazimuth bin. Note that the observed backazimuths for each event at frequency $\theta_k(f)$ were used rather than the theoretical great circle. For each frequency, the best values of C_0, A and θ_0 that fit the phase-velocity measurements obtained in each backazimuth bin were sought using an L1 norm misfit function F_3. We tested a number of weighting schemes: (1) no weighting; or weighting by (2) the number of $(\Delta t_{ij}^k(f), D_{ij}^k(f))$ data points (represented by the greyscale bar in Figs 5, 7, 9 and 11); (3) the fit F_2 corresponding to the consistency between the events in one azimuth bin and (4) the inverse of the velocity error bars calculated by eq. (1) and shown in Figs 5, 7, 9 and 11. Uncertainty in C_0, A and θ_0 are estimated as the maximum and minimum values of each parameter for which the fit is 5 per cent larger than the minimum F_3, whilst holding the two other parameters at their estimated optimum value.

3 ANISOTROPY RESULTS

3.1 Shear wave (*SKS*) splitting

As was described previously for the centrally located station at the Ekati Diamond Mine™ (EKAT) (Snyder *et al.* 2003), *SKS* splitting

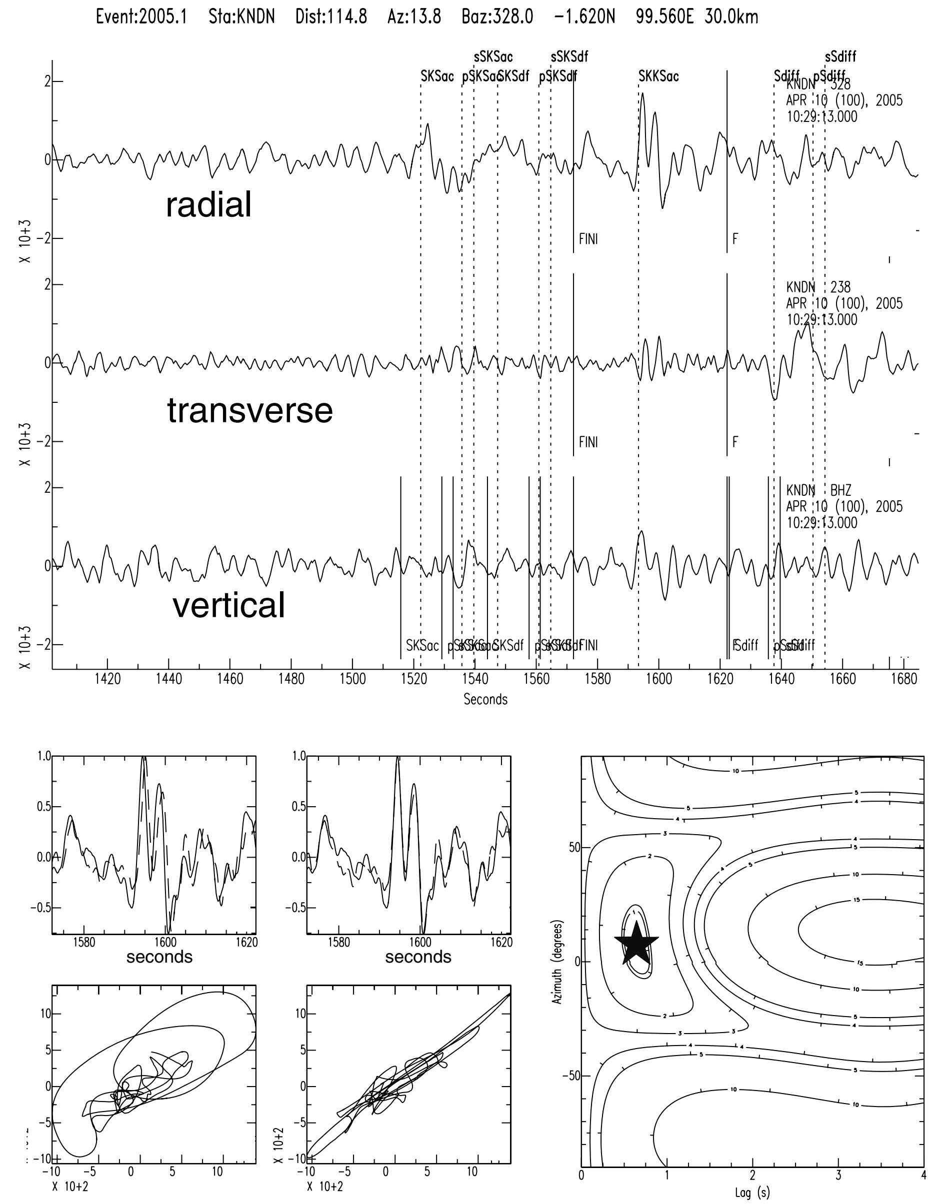

Figure 2. (*Continued.*)

parameters show systematic variations with backazimuth (Fig. 3) and this variation is diagnostic of layered anisotropy rather than homogeneous or dipping mantle fabric (Silver & Savage 1994; Rümpker & Silver 1998; Rümpker *et al.* 1999; Saltzer *et al.* 2000). The observed azimuthal variations of delay times and fast polarization directions are similar among the 25 stations studied and also with theoretical variations (Silver & Savage 1994) due to two horizontal layers of distinct anisotropy (Fig. 3, Table 4). At each station, observed backazimuthal variations in the two splitting parameters were simultaneously compared with the theoretical variations to determine a best match. Two of the four splitting parameters needed to define two horizontal layers of anisotropy can be estimated analytically (Rümpker *et al.* 1999) by identifying minima in delay times that occur near nodal azimuths where both splitting parameters vary greatly with small changes in azimuth. A minimum in delay time theoretically occurs at the null direction (either the fast or slow polarization direction) of the principal anisotropy layer and the value thus represents the magnitude of splitting occurring within the secondary anisotropy layer. These two analytical estimates expedite a grid search for all four splitting parameters (Table 4). The resulting best-fitting, two-layer models were contrasted with a single layer (homogeneous) model by comparing estimated chi-squared misfit of each model to the observations for each station using all reliable azimuthal bins available for that station (N). Only the one-layer misfits for δt variation at stations GLWN, DSMN and YKW clearly surpass the misfit for a two-layer model (Table 4). The consistency between all of the preferred two-layer models across this large array is noteworthy and unusual globally. The close fit of a two-layer model obviated investigations of three or more layers (Saltzer *et al.* 2000; Menke & Levin 2003).

Although two-layer anisotropy was consistently indicated throughout the Slave Array (compare also EKTN and YKW in Fig. 3b), the observed splitting and indicated anisotropy were strongest within the Lac de Gras kimberlite field surrounding the

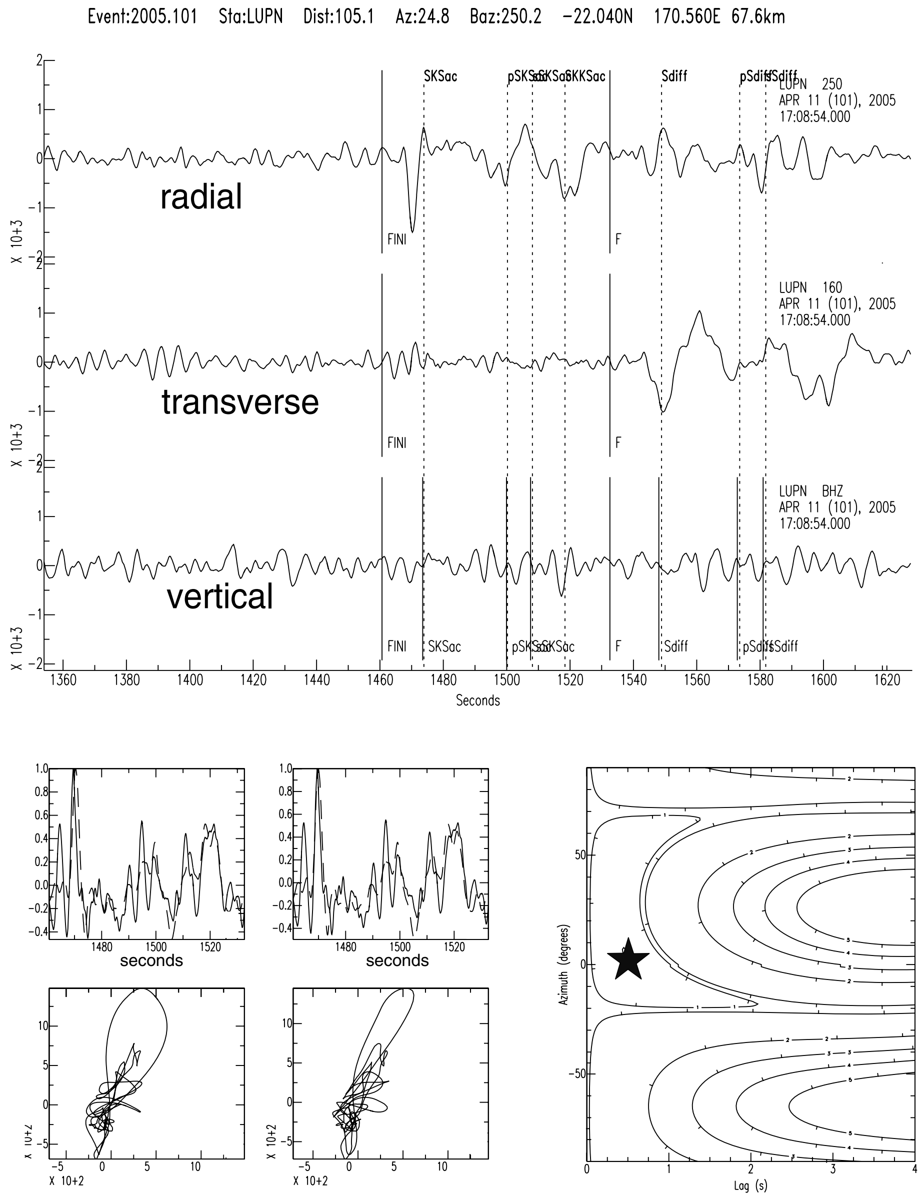

Figure 2. (*Continued.*)

Ekati Diamond Mine™ as represented by stations DVKN, LDGN, EKTN, YMBN, ACKN and YNEN. Northward systematic decreases in $\delta t1$ values occur at stations COWN and LUPN (Fig. 3d) and similarly in the far south at stations SNPN and IHLN (Fig. 3h). Variation in fast polarization direction ($\phi 1$) is less distinct, but LUPN is distinct at 65° from the 50°–52° typical in the centre of the array to the 35°–45° typical of the southern third of the array (Table 4). The fast polarization direction within the secondary anisotropic layer ($\phi 2$) is variable but strikes within 10° of north throughout most of the centre of the array.

3.2 Rayleigh wave studies

The analysis described above was carried out on the entire array of broad-band POLARIS and YKW stations, as well as on subarrays within subdivisions of the craton (Central Slave, Southeast Slave and Southwest Slave) previously outlined using properties of mantle xenolith samples. For each (sub)array, phase velocities determined for each backazimuth window (Figs 5, 7, 9 and 11) yielded estimates of mean phase velocity C_0 (panel a of Figs 6, 8, 10 and 12), per cent anisotropy A (panel b of Figs 6, 8, 10 and 12) and fast polarization direction θ_0 (panel c of Figs 6, 8, 10 and 12), each varying with surface wave periods that map to different depth sensitivities. When C_0 is very different from the isotropic velocity for the array, the different weighting schemes give different results, or anisotropy parameters are computed from a small number of data with a bad azimuthal distribution, the anisotropy is considered unresolved and the values are not shown in the figures.

The mean phase velocities are generally well resolved as a function of backazimuth between periods of 20 and 150 s using all (sub)arrays (Figs 6a, 8a, 10a and 12a). The pronounced heterogeneity of station distribution when considering the entire Slave Array makes the derived anisotropy and fast polarization estimates suspect (Figs 6b and c). In contrast, the Southeast Slave subarray has the most uniform station distribution and our analysis reveals a clear trend in the fast polarization direction (θ_0), from 0 to 060° as period

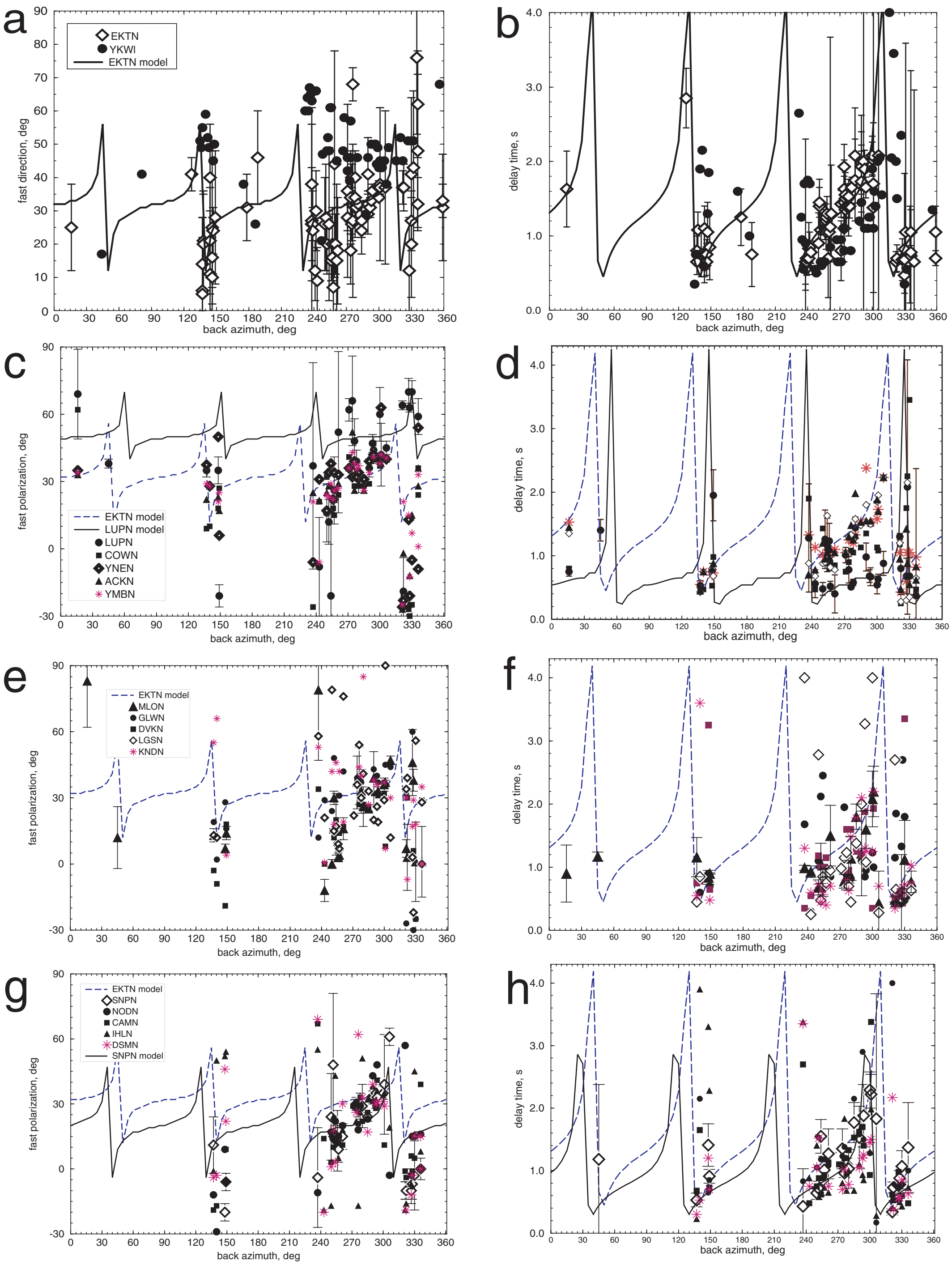

Figure 3. Variation of *SKS*/*SKKS* splitting parameters with respect to backazimuth. Plots on the left (a, c, e, g) show the variation of fast polarization direction (ϕ); those on the right (b, d, f, h) show variation in delay time or lag (δt). Stations are generally grouped together progressively north to south. Error bars are illustrated for one station set in each plot. Solid and dashed lines are variations predicted for two layers of anisotropy beneath the indicated station (Table 4) using the method of Silver & Savage (1994).

increases (Fig. 8c). Note that error bars are large at short periods and that anisotropy estimates (A) of <3 per cent cannot exclude isotropic behaviour at periods less than 90 s (Fig. 8b). The strongly linear Central Slave subarray yielded less clear results (Figs 9 and 10). The only well-resolved cluster of fast directions occurs between periods of 60 to 140 s at $\theta_0 \sim 330^\circ$ (indicated as -30° in Fig. 10c), collinear with the trend of the array (Fig. 1). The 045° trends from the *SKS* splitting analysis in this region are not apparent here, but poorly resolved trends around 000° with 2–3 per cent anisotropy appear at periods of 20–80 s. The Southwest Slave subarray did not produce stable results (Figs 11 and 12); at periods less than 70 s, the estimate of a fast polarization around 050° with about 2 per cent anisotropy is similar to one fast polarization given by *SKS* analysis at station YKW.

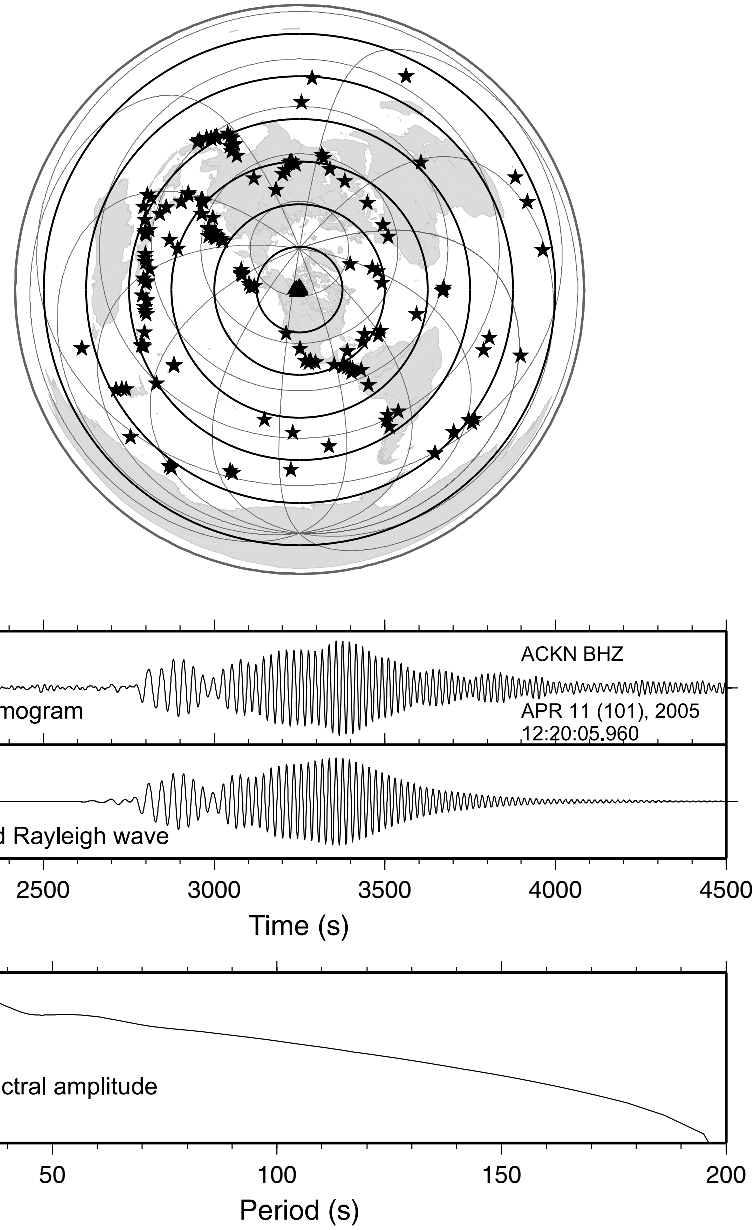

Figure 4. (a) Map of the 170 events used for the Rayleigh wave analysis (stars), centred on the array (triangle), the frequency range used in analysis depends on the location of the earthquake (epicentral distance, oceanic or continental path, depth) and on its magnitude. (b) Example of the Rayleigh data set: signal recorded at ACKN for a M 6.7 earthquake in Papua New Guinea; top panel: raw signal, bottom panel: extracted fundamental mode Rayleigh wave. (c) Logarithmic spectral amplitude of the extracted Rayleigh wave showing a good quality signal from 20 to 190 s.

4 INTERPRETATION, MODELLING AND DISCUSSION

4.1 Joint interpretation

Joint interpretation of *SKS–SKKS* splitting and Rayleigh wave anisotropy within the central Slave craton represents a rare opportunity because of the rich relevant petrological and geochemical database available. This is due to the numerous kimberlite pipes whose mantle xenoliths and garnet xenocrysts were analysed during intense exploration for diamonds in this region over recent decades. First, we will attempt to reconcile the estimates of seismic anisotropy from the two methods presented here. Forward modelling of Rayleigh wave anisotropy based on assumptions from the *SKS* observations will follow. Finally, independent petrological constraints will be considered and integrated with tectonic implications of the results.

Anisotropy parametrization using near-vertically propagating *SKS* or *SKKS* waves provides information about polarization in the horizontal plane (perpendicular to shear wave propagation), whereas parametrization using Rayleigh waves provides information about polarization in the vertical plane containing source and receiver, principally the vertical component. The Rayleigh wave analysis also provides the only formal depth constraints on seismic anisotropy. By jointly interpreting the parameters resulting from the same station array, a 3-D estimate of anisotropy is possible.

In most cases investigated worldwide to date, results of joint interpretation were inconsistent. This is also true for most of the Slave

Table 4. One- and two-layer models used to match the shear wave splitting data.

		Two-layer models						One-layer models			
Station	N	$\phi 1$	$\delta t1$	$\phi 2$	$\delta t2$	X(δt)	X(ϕ)	$\langle\phi\rangle$	$\langle\delta t\rangle$	X(δt)	X(ϕ)
LUPN	22	65	0.39	40	0.24	0.072	0.002	39	0.815	0.122	0.00
COWN	22	52	0.75	3	0.28	0.032	0.108	24	0.86	0.053	0.117
YNEN	21	50	1.10	−5	0.30	0.019	0.094	31	1.1	0.125	0.157
ACKN	21	51	1.20	−5	0.48	0.035	0.108	24	1.18	0.077	0.168
YMBN	21	51	0.92	23	0.41	0.010	0.054	31	1.16	0.062	0.052
GLWN	25	65	0.80	29	0.28	0.234	0.239	21	1.17	0.151	0.482
EKTN		52	1.02	6	0.41						
LDGN	21	50	0.66	−4	0.50	0.084	0.264	21	1.06	0.122	0.284
DVKN	21	58	0.90	17	0.65	0.031	0.175	20	1.09	0.066	0.152
LGSN	22	45	0.68	10	0.44	0.055	0.217	22	1.07	0.256	0.228
MLON	29	40	0.70	5	0.38	0.088	0.298	13	1.03	0.095	0.572
BOXN	29	47	0.50	5	0.30	0.102	0.400	18	1.05	0.131	0.314
MGTN	18	35	0.52	15	0.20	0.072	0.134	21	0.88	0.085	0.140
KNDN	20	52	0.48	17	0.35	0.097	0.137	33	0.94	0.140	0.126
NODN	22	35	0.70	−5	0.22	0.064	0.350	12	1.15	0.110	0.594
CAMN	24	45	0.69	−10	0.40	0.124	0.079	10	1.00	0.141	0.637
SNPN	29	40	0.68	−4	0.30	0.031	0.138	13	0.84	0.159	0.434
IHLN	26	37	0.40	25	0.25	0.410	0.390	19	1.16	0.258	0.460
DSMN	22	52	0.72	−9	0.34	0.146	0.009	15	0.95	0.095	0.022
YKW3	54	66	0.80	25	0.36	0.264	0.022	47	1.31	0.132	0.072
CTLN	18	85	1.1	0	0.42	0.107	0.079	50	1.42	0.094	0.064
GALN	18	55	0.7	18	0.32	0.125	0.318	19	0.97	0.153	0.488

N is the number of backazimuthal bins used in the modelling; ϕ is the modelled fast apparent anisotropy direction (in degrees) for layers 1 and 2; δt is the delay or splitting time (in seconds) for layers 1 and 2; $\langle\phi\rangle$ is the average fast apparent anisotropy direction observed at that station presumed to characterize one homogeneous layer; $\langle\delta t\rangle$ is the average delay; X (δt) and X (ϕ) are the chi-square goodness of fits for the various splitting parameters to the observations. EKTN parameters described in Snyder *et al.* (2003).

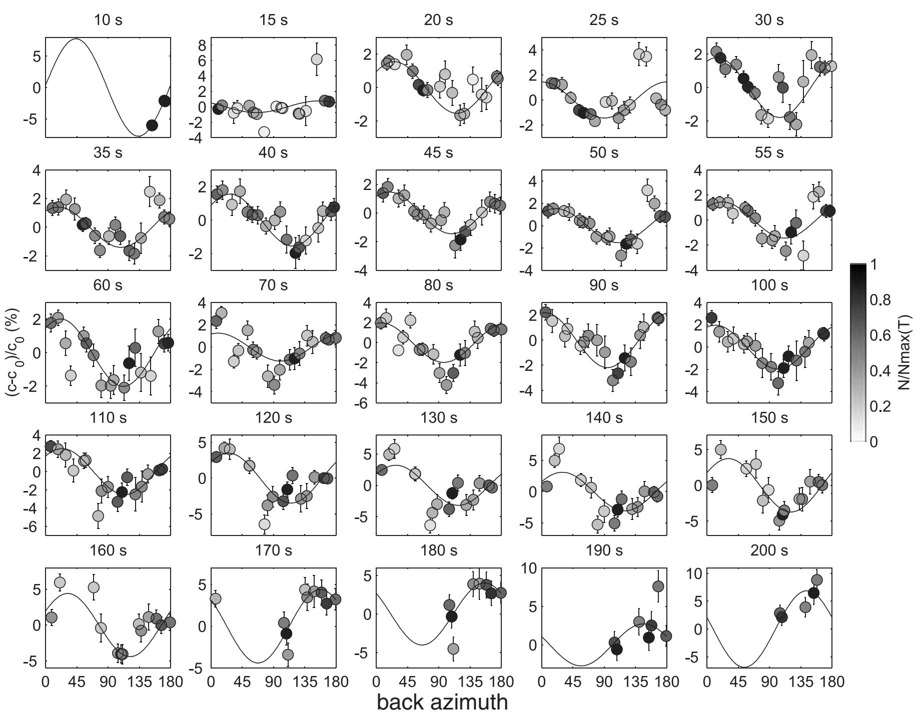

Figure 5. Rayleigh-wave phase velocity versus backazimuth for each wave period indicated using the entire Slave Array. The shade of each dot indicates the number of $(\Delta t_{ij}^{k}(f), D_{ij}^{k}(f))$ points divided by the maximum number for that period. The cosine (solid line) is obtained by weighting the points by the inverse of the error bars (values on Fig. 6).

Array with the notable exception of the Southeast subarray that has the most homogeneous station distribution. Fast Rayleigh wave polarizations within the Southeast subarray rotate nearly linearly from 000 ($\pm$41)$^\circ$ at 30 s period (Moho depth, 40 km) to 060 ($\pm$17)$^\circ$ at 160 s ($\sim$200 km) (Fig. 10c) with related anisotropy increasing from 1 to 6–9 per cent (Fig. 8b). Fast polarizations from *SKS* waves recorded at these same eight stations indicate one layer with an average 041° trend and another with 006° trend. Discontinuities in

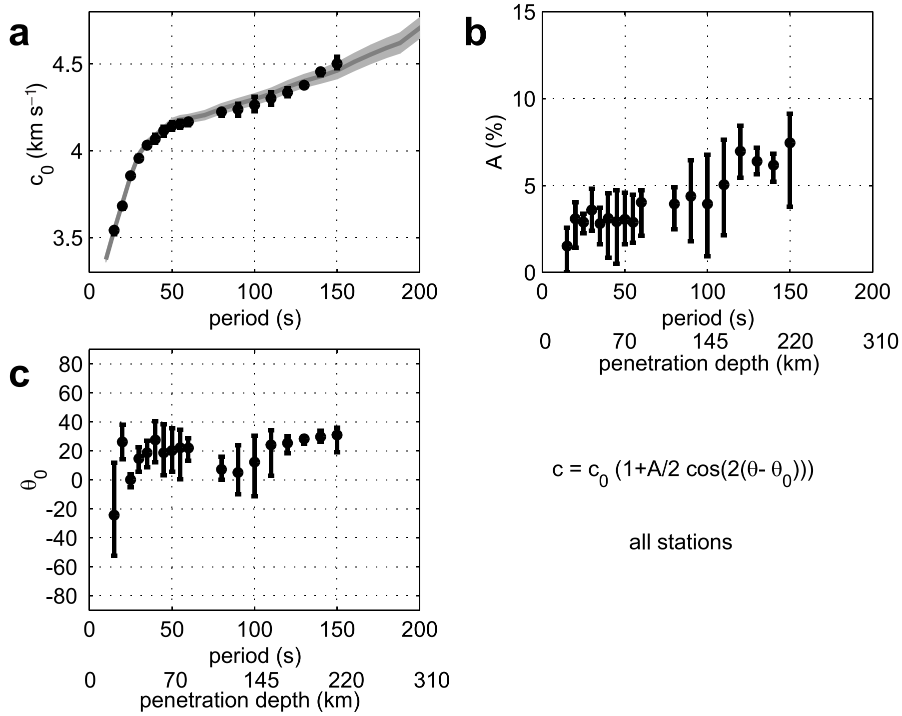

Figure 6. Anisotropy parametrization from analysis of Rayleigh waves across the entire Slave array. (a) The black line is the average phase velocity $C_0(f)$ determined from all azimuthal windows; the grey area represents the isotropic phase velocity before consideration of azimuthal dependence, see text. (b) Apparent peak-to-peak percentage of anisotropy and its uncertainty. (c) Fast polarization direction of anisotropy and its uncertainty. The values presented are obtained by weighting the points by the inverse of the error bars presented on Fig. 4. Dubious points are not shown in the figure (see text).

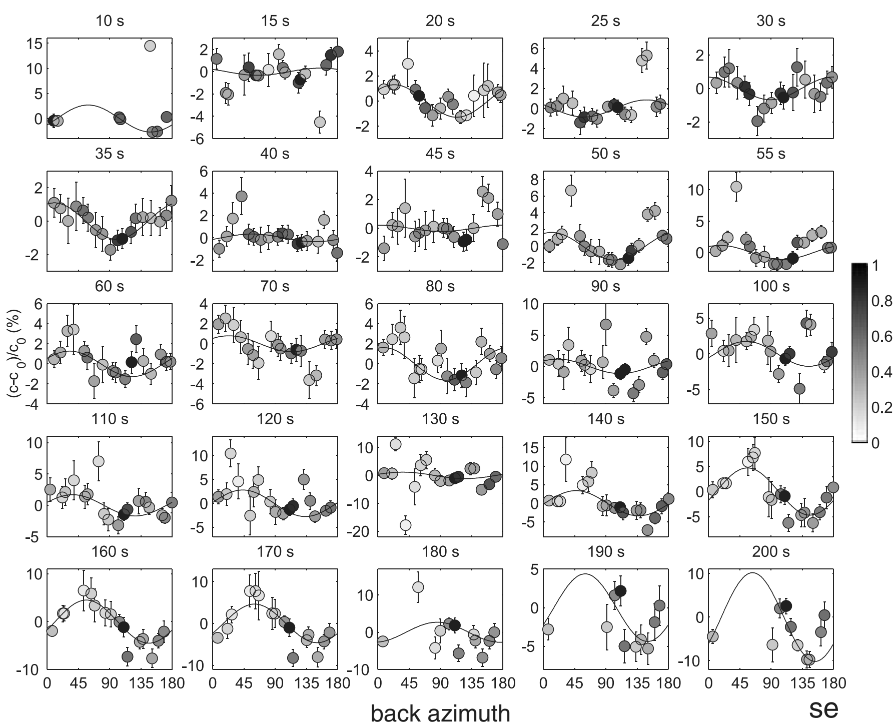

Figure 7. Phase velocity plots as in Fig. 5 but using only Southeast subarray stations (Fig. 1).

seismic anisotropy revealed by transverse components of deconvolved impulse response (Bostock 1998) beneath these stations indicate a layer boundary at 140–160 km (Snyder *et al.* 2004) equivalent to a Rayleigh wave period of 100–130 s. The joint interpretation is thus fully consistent with a two-layer mantle model in which an uppermost mantle layer has a north-trending anisotropy and a second layer, located at 150 to 200 km depths, has a northeast-trending anisotropy. The observed average delay times from *SKS* splitting of

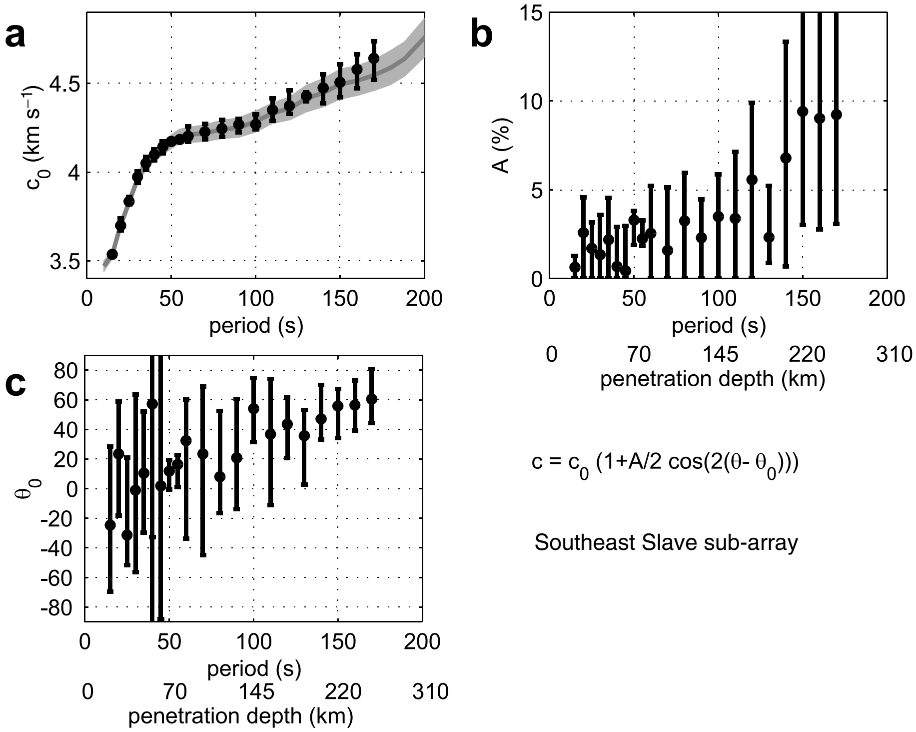

Figure 8. Anisotropy plots as in Fig. 6 but using only Southeast subarray stations.

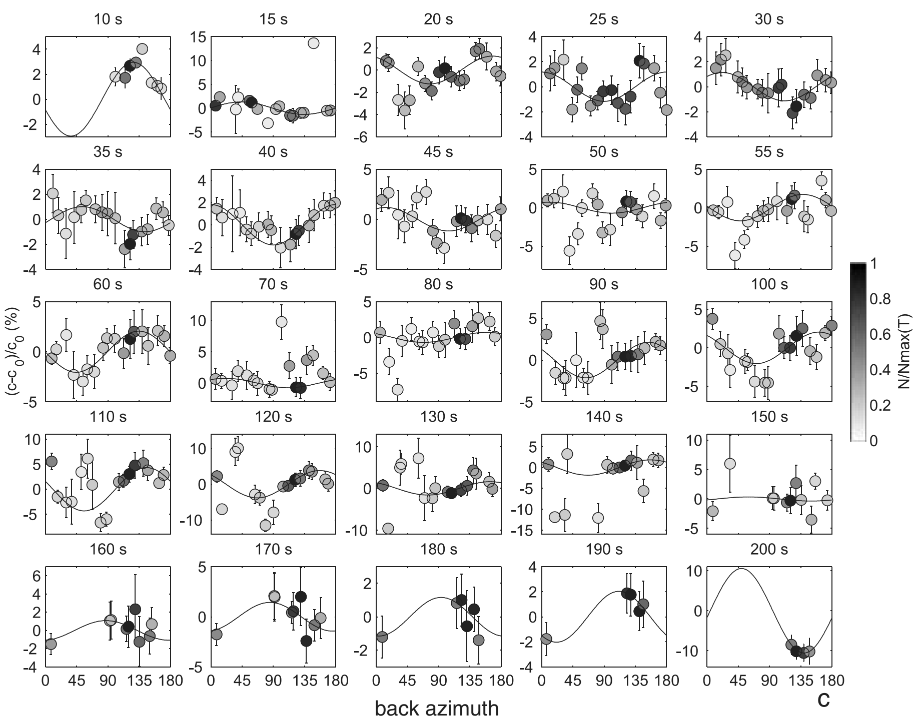

Figure 9. Phase velocity plots as in Fig. 5 but using only Central subarray stations (Fig. 1).

0.30 and 0.58 s for the two layers are consistent with approximately 2 and 5 per cent anisotropy, respectively, within layers 50 km thick. These values are again consistent with anisotropies derived from Rayleigh wave dispersion; the calculated anisotropies >7 per cent at periods >130 s imply even higher *Vs* anisotropy, which is petrologically unrealistic for mantle layers only tens of kilometres thick (Kopylova & Caro 2004).

Average delay times of 0.3–0.4 s everywhere within the upper layer are consistent with estimates of 2–3 per cent anisotropy from petrological considerations (Kopylova & Caro 2004) and with anisotropy estimated from Rayleigh waves of less than 90 s periods (Figs 6b and 8b). Stations of the Central subarray have average *SKS* delay times in the deeper layer about twice those of the Southeast subarray (Table 4, Fig. 1). Anisotropies estimated from Rayleigh

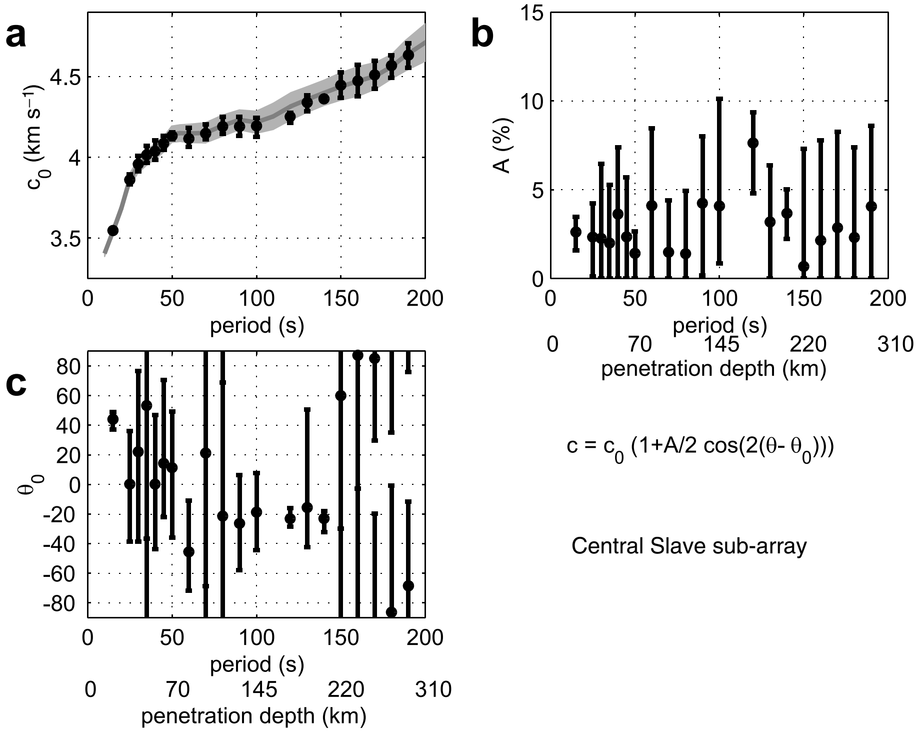

Figure 10. Anisotropy plots as in Fig. 6 but using only Central subarray stations.

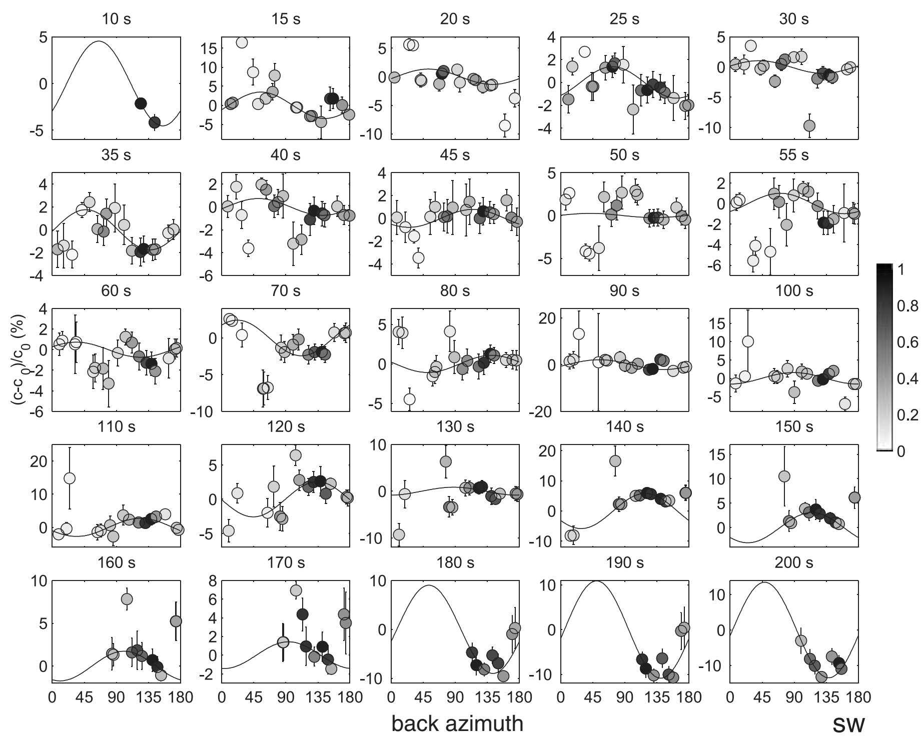

Figure 11. Phase velocity plots as in Fig. 5 but using only Southwest subarray stations (Fig. 1).

waves are greater, but less consistent than those from the Southeast subarray. Rayleigh waves with periods of 60–140 s indicate a possible third, middle layer with higher anisotropy (Fig. 8), but such a layer is discounted due to the coincidence of the polarization, the subarray trend and the inconsistency with *SKS* splitting results.

The Central subarray coincides closely with the Lac de Gras kimberlite field, and stockworks of vertical sheeted dykes that fed the kimberlite eruptions can explain the observed *SKS* splitting parameters related to the deeper mantle layer as due to structural preferred orientation (SPO) (Snyder & Lockhart 2005). If this interpretation is correct and applicable to the entire Slave craton, then the mantle

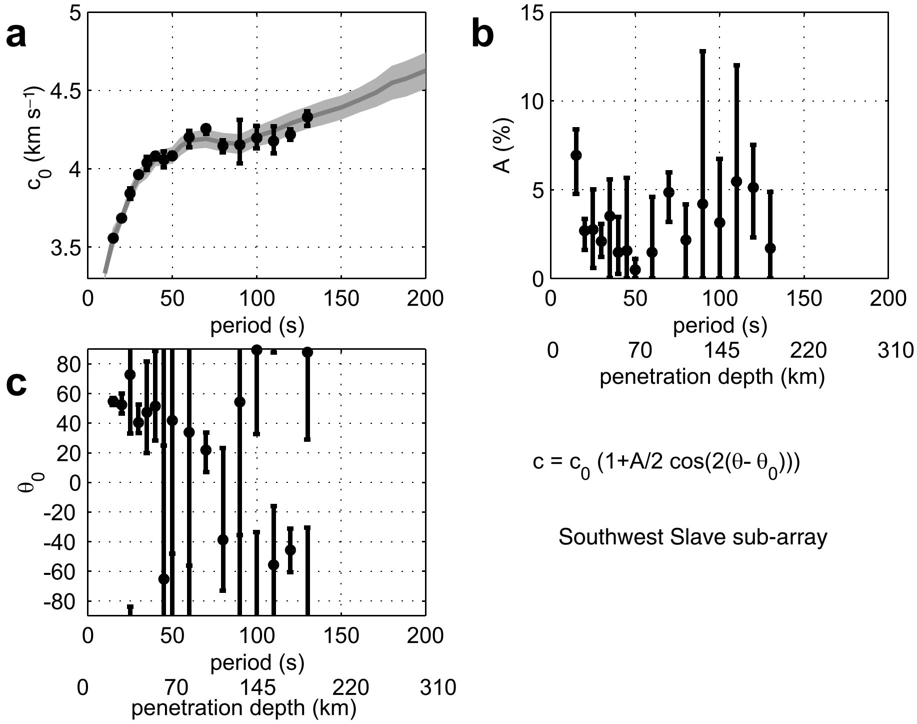

Figure 12. Anisotropy plots as in Fig. 6 but using only Southwest subarray stations.

beneath the Southeast subarray would contain roughly 2/3 as many dykes. If the anisotropy within the lower layer beneath the Southeast subarray is instead entirely due to lattice preferred orientation (LPO) related to present-day plate motion (e.g. Bank *et al.* 2000), then the Lac de Gras feeder dykes produce roughly 2/3 of the total anisotropy within the lower layer beneath the Central subarray.

4.2 Forward modelling

Consistency between the SKS and Rayleigh wave estimates of polarization direction and degree of anisotropy were further investigated via forward modelling of Rayleigh wave anisotropy from mantle properties. Rayleigh wave anisotropy was computed using modelling code developed by Thomson (1997) designed to propagate waves in layered media with any 3-D anisotropy. A background isotropic shear wave velocity model was derived from linear inversion of the average dispersion curve for the Southeast Slave subarray (using SURF96 from Herrmann & Ammon 2004). Depth-dependent azimuthal anisotropy was added onto this isotropic velocity model. Following Pedersen *et al.* (2006), we used the elastic coefficients of an olivine crystal but averaged the slow (b and c) axes to get a symmetry around an a-axis kept horizontal. The *Vs* azimuthal anisotropy of this new model is 7.84 per cent. Therefore, to have a layer with 3 per cent *Vs* anisotropy, we added 0.38 times this particular anisotropy to the isotropic model; this is equivalent to saying that 38 per cent of the rock is composed of olivine crystals oriented in the same direction. A layer with 10 per cent *Vs* anisotropy requires a factor of 1.28, and more than 100 per cent of the rock has to be composed of oriented olivine crystals, that is, such a *Vs* anisotropy cannot be explained by LPO only.

We tested three different kinds of anisotropy variation with depth based on the *SKS* splitting results described here and on three inferred geodynamic hypotheses. For each anisotropic model, the phase velocity of the first mode encountered (generally the Rayleigh fundamental mode) was computed for azimuths between 0° and 180° and periods between 20 and 180 s using the method of Thomson (1997) and Martin & Thomson (1997). From each period the parameters of the Rayleigh azimuthal anisotropy (average velocity C_0, anisotropy A and fast direction θ_0) were estimated by fitting a cosine curve to the velocity points using an L1 norm.

In the central Slave, *SKS* splitting analysis showed two anisotropic layers with different polarizations; one was attributed to a vertical dyke swarm at 110–190 km depths (Snyder & Lockhart 2005). The first Earth model tested has three anisotropic regions: from the Moho to 110 km where the uppermost lithosphere was assigned an anisotropy of 3 per cent with a horizontal fast direction at 010°; from 110 to 190 km the lower lithosphere had an anisotropy of 10 per cent with a horizontal fast direction of 050°; from 190 to 280 km depth the asthenosphere had an anisotropy of 5 per cent with a horizontal fast direction of 050° (Fig. 13a). The resulting Rayleigh phase velocity anisotropy varies smoothly in amplitude and direction even where modelled *Vs* anisotropy varies sharply (Figs 13b and c). The maximum calculated amplitude of ~5.5 per cent is a little less than half of the 10 per cent input. At longer periods the upper layer still influences the estimates and the fast direction never reaches the 050° value input for *Vs* anisotropy below 110 km, in particular when estimated through a cosine fit.

Within the Southeast subarray the *SKS* results show directions similar to the Central subarray for the fast polarization but lower amplitudes of anisotropy and delay. The second Earth model therefore used the same upper lithosphere and asthenosphere as in the previous model but had a lower lithosphere with only 5 per cent *Vs* anisotropy in the 050° direction (Fig. 14a). The hypothesized tectonic model assumed anisotropy derives from olivine LPO in two distinct stacked lithospheric slabs (Bostock 1998; Davis *et al.* 2003). The results are similar to the previous model, but with lower amplitude (3.5 per cent) of the calculated anisotropy (Fig. 14c).

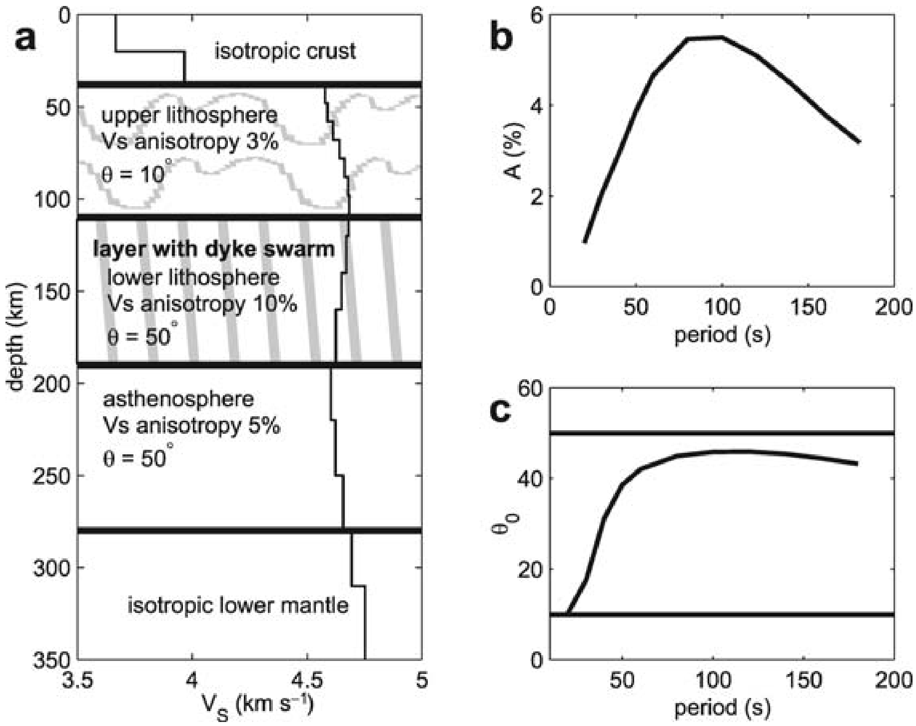

Figure 13. Input model to test kimberlite dyke swarm hypothesis (a) and the output Rayleigh anisotropy parameters of (b) apparent peak-to-peak percentage of anisotropy, and (c) fast polarization direction. In (c) polarizations at 010° and 050° are repeated from the input model (a). The dyke swarm is assumed to consist of 22 dykes, each 300–1000 m wide, with a strong *Vs* contrast (5000 m s^{-1} versus 2800 m s^{-1}).

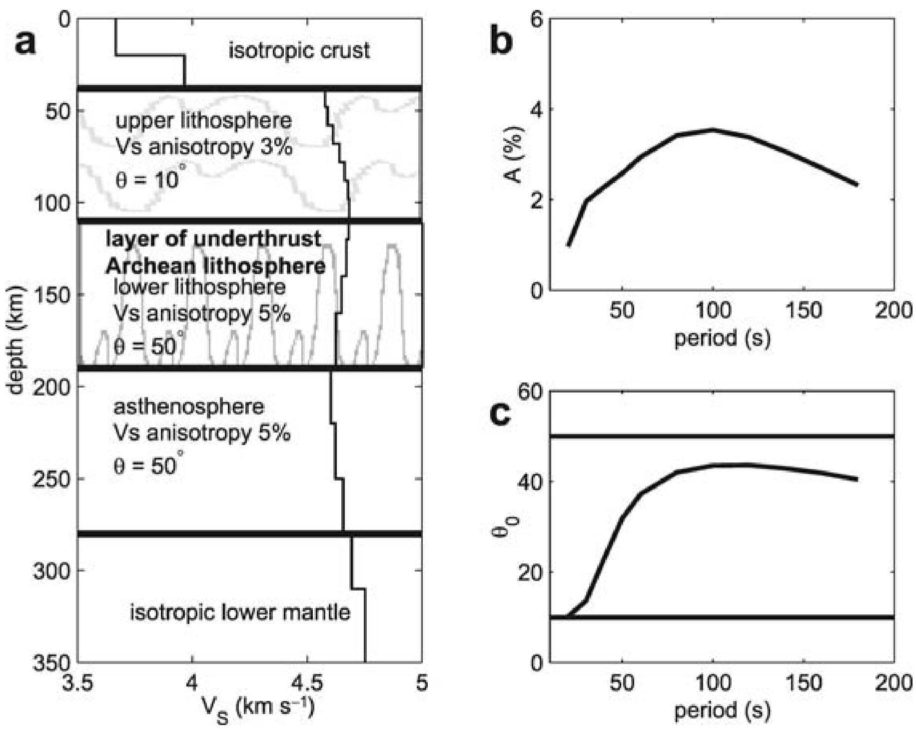

Figure 14. Input model to test lithosphere stacking hypothesis and the output Rayleigh anisotropy parameters, presented as in Fig. 13.

The third model tested a competing hypothesis, that an Archaean plume caused the anisotropy in the lower Slave lithosphere (Griffin *et al.* 1999). This model was composed of a thinner upper lithosphere, with assumed 3 per cent anisotropy in the 010° direction to 70 km depth, underlain by an isotropic middle layer down to 150 km depth and a lower lithosphere with 5 per cent anisotropy in the 050° direction from 150 to 200 km (Fig. 15a). The asthenosphere is again given a 5 per cent anisotropy in the 050° direction down to 280 km. The thick isotropic region in the middle lithosphere produces a minimum in the amplitude of the Rayleigh wave anisotropy

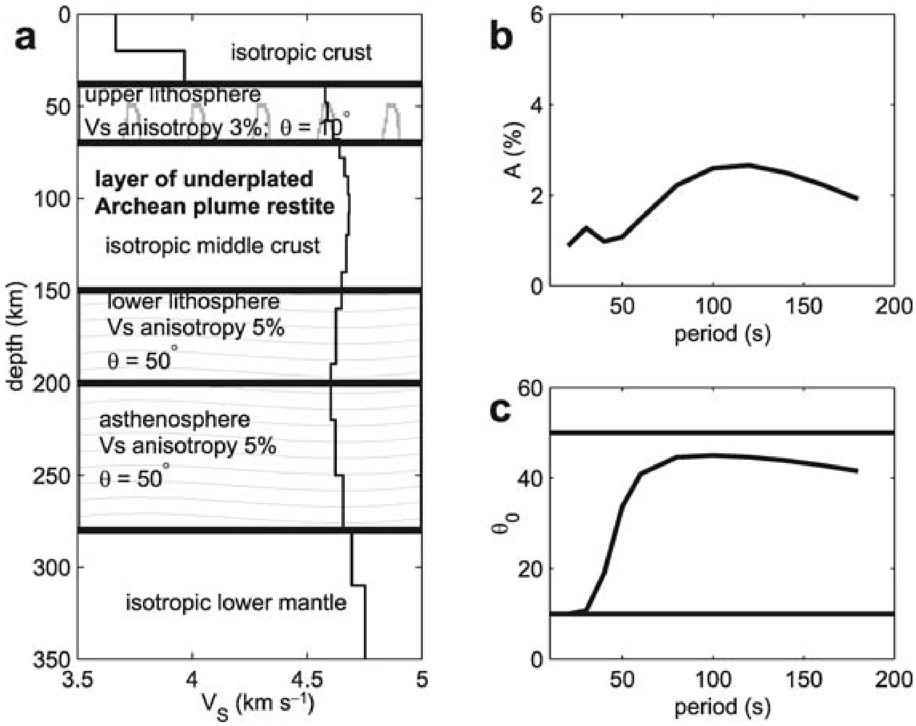

Figure 15. Input model to test Archaean mantle plume hypothesis and the output Rayleigh anisotropy parameters, presented as in Fig. 13.

and a sharper transition in the fast polarization direction (Figs 15c and d).

Direct analysis of the Rayleigh waves suggested that the Southeast Slave has a strong anisotropy in the deep lithosphere or asthenosphere, but the amount of Rayleigh wave anisotropy observed at periods of 140–170 s cannot be entirely explained by petrologically reasonable amounts of *Vs* anisotropy produced by LPO of olivine in a horizontal plane. Therefore, exploring the influence of 3-D variations in anisotropy is important. For periods up to 130 s, the amount of anisotropy observed is comparable to that obtained in the forward modelling, but the resolution is not sufficient to discriminate between the three different hypotheses tested. Observations of fast directions around 005° at periods less than 55 s indicate that the upper anisotropic layer extends deeper than 80 km.

4.3 Cause of anisotropy

Beneath the eight stations of the Southeast Slave array, where both the *SKS* splitting and Rayleigh wave anisotropy parameters are most consistent and reliable, a coherent 3-D model of mantle seismic anisotropy can be inferred. The consistency of fast polarization directions and of anisotropy inferred from *SKS* delays and phase velocity variation is fully consistent with the principal anisotropy axis nearly horizontal and pointing roughly north to northwest. The relative amplitudes of the other two axes remain unknown, but these can be assumed to be similar and significantly less than the principal one. Underlying assumptions of a hexagonal symmetry system with a horizontal axis used in the *SKS* splitting analysis thus appear justified in this case and may partly explain the 'well-behaved' layered anisotropy observed in the Slave craton. If a vertical dyke swarm beneath the Lac de Gras kimberlite field is as hypothesized, it may cause lateral variations in the amplitude such as those observed between subarrays, but not the overall consistency of the observed seismic anisotropy.

Anisotropies of 2–4 per cent with a northerly fast polarization within the uppermost 80–120 km are petrologically reasonable and geologically consistent with the principal phase of Archaean deformation that affected the Slave craton at 2610–2580 Ma. This so-called D2 deformation resulted in regional-scale open folds with generally north–south axes throughout the upper crust and presumably at depth (Bleeker *et al.* 1999; Davis *et al.* 2003). Archaean proto-continental lithosphere of this age is modelled to have thicknesses of 90–120 km (Grotzinger & Royden 1990) and the pervasive plutonism related to Prosperous Group granite emplacement that affected the crust of the Slave craton during this period would be consistent with melt depletion within the underlying uppermost mantle that produced the ultradepleted harzburgitic layer indicated by xenolith studies (Griffin *et al.* 1999; Kopylova & Caro 2004).

The deeper layer of anisotropy is more complex and controversial in its origin. A strong possibility is that a second Archaean lithosphere thrust beneath and along the approximately 80–120 km base of the upper layer and contained a similar but distinct anisotropy. Underthrusting would have both generated the melt described above and effectively doubled the lithosphere by 2500 Ma. A layer created by underplated material from a nearby plume (Griffin *et al.* 1999) remains equally viable. The lower part of this layer and the asthenosphere have fast polarizations aligned with present-day North America plate motion (Bank *et al.* 2000) that suggests mechanisms such as olivine LPO are as important here as previously suggested globally (e.g. Vinnik *et al.* 1992; Debayle & Kennett 2000). Kimberlite dyke emplacement may enhance this anisotropy locally (Snyder & Lockhart 2005). A strongly layered mantle was recognized beneath station YKW (Bostock 1998) and this station has *SKS* splitting parameters similar to most stations in the central Slave craton. Subducted Proterozoic-age lithosphere may therefore underlie much of the Slave craton and contribute another distinct seismic anisotropy.

5 CONCLUSIONS

The seismic anisotropy of the subcontinental mantle lithosphere of the Slave craton appears strong and unusually well ordered in that it occurs in two distinct layers and is consistently parametrized as such by independent anisotropic analyses of *SKS* and Rayleigh waves. The layered anisotropy correlates with petrologically distinct layers 50–150 km thick that were previously predicted by geochemical analysis of xenoliths and xenocrysts brought to the surface in kimberlite eruptions, but our forward modelling supports the hypothesis that structural preferred orientation of these kimberlite dykes may locally augment the seismic anisotropy observed within the known kimberlite fields of the central Slave craton over anisotropy expected from lattice preferred orientation of mineral assemblages as observed throughout all other parts of the craton studied to date. About 0.4 s of observed delay time in SKS arrivals can be attributed to the upper lithosphere (0–120 km) as relict LPO and SPO related to regional D2 folds observed at the surface. Our modelling indicates that 0.5 s of delay is due to SPO in kimberlite dyke swarms that fed the Lac de Gras kimberlite field; another 0.4 s of delay is LPO in the deepest lithosphere associated with North America plate motion. The Slave craton is relatively small on a global scale and has a relatively simple tectonic history compared to other well-studied cratons so that its well-ordered anisotropy is not unexpected. The variable strength of the anisotropy is significant in that it indicates both lattice- and structural-preferred-orientations act as possible sources and it makes the Slave craton an important reference for future global studies of seismic anisotropy or subcontinental mantle lithosphere.

ACKNOWLEDGMENTS

C.J. Thomson was a key contributor to this research, in many ways. The research presented here benefited from help from numerous sources, among them: members of the POLARIS consortium (especially I. Asudeh and C. Andrews for their efforts in installing and maintaining seismic stations), C. Relf of the NWT Geoscience Centre (Yellowknife, NWT), W. Bleeker, M. Bostock, W. Davis, H. Grütter, Alan Jones, G. Lockhart and S. Rondenay. This work was funded under Letters of Agreement among the Geological Survey of Canada, BHP-Billiton Diamonds Inc.; DeBeers Canada Inc.; Indicator Minerals Inc.; Kennecott Canada Exploration Inc.; Shear Minerals Ltd.; and Stornoway Diamond Corp. POLARIS equipment was purchased through a Canadian Foundation for Innovation grant. Geological Survey of Canada contribution 2005785, to its Northern Resource Development Program.

REFERENCES

Babuška, V. & Cara, M., 1991. *Seismic Anisotropy in the Earth*, Kluwer Academic Pub., Dordrecht, the Netherlands, 217 pp.

Bank, C.-G., Bostock, M.G., Ellis, R.M. & Cassidy, J.F., 2000. A reconnaissance teleseismic study of the upper mantle and transition zone beneath the Archean Slave craton in NW Canada, *Tectonophysics,* **319,** 151–166.

Bleeker, W.J., Ketchum, W.F., Jackson, V.A. & Villeneuve, M., 1999. The Central Slave Basement Complex, Part I: its structural topology and autochthonous cover, *Can. J. Earth Sci.,* **36,** 1083–1109.

Bostock, M.G., 1998. Seismic stratigraphy and evolution of the Slave province, *J. geophys. Res.,* **103,** 21 183–21 200.

Brisbourne, A., Stuart, G. & Kendall, J.-M., 1999. Anisotropic structure of the Hikurangi subduction zone, New Zealand—integrated interpretation of surface-wave and body wave observations, *Geophys. J. Int.,* **137,** 214–230.

Darbyshire, F.A. & Asudeh, I., 2006. Generic instrument responses for the POLARIS and FedNor seismograph network in Canada, Geological Survey of Canada Open File Report 5185, 22 pages.

Davis, W.J., Jones, A.G., Bleeker, W. & Grutter, H., 2003. Lithospheric development in the Slave craton: a linked crustal and mantle perspective, *Lithos,* **71,** 575–589.

Debayle, E. & Kennett, B.L.N., 2000. Anisotropy in the Australian upper mantle from Love and Rayleigh waveform inversion, *Earth planet. Sci. Lett.,* **184,** 339–351.

Debayle, E., Kennett, B.L.N. & Priestley, K., 2005. Global azimuthal seismic anisotropy and the unique plate-motion deformation of Australia, *Nature,* **433,** 509–512.

Gaherty, J.B., 2004. A surface wave analysis of seismic anisotropy beneath eastern North America, *Geophys. J. Int.,* **158,** 1053–1066.

Griffin, W.L. *et al.*, 1999. Layered mantle lithosphere in the Lac de Gras area, Slave Craton: composition, structure, and origin, *J. Petrol.,* **40,** 705–727.

Grotzinger, J. & Royden, L., 1990. Elastic strength of the Slave craton at 1.9 Gyr and implications for the thermal evolution of the continents, *Nature,* **347,** 64–66.

Grütter, H.S., Apter, D.B. & Kong, J., 1999. Crust-mantle coupling: evidence from mantle-derived xenocrystic garnets, in *Proc. 7th kimberlite conference*, pp. 307–312, eds Gurney, J.J. & Richardson, S.R., Red Roof Designs, Cape Town.

Heaman, L.M., Creaser, R.A., Cookenboo, H.O. & Chacko, T., 2006. Multistage modification of the northern Slave mantle lithosphere: evidence from zircon- and diamond-bearing eclogite xenoliths entrained in Jericho kimberlite, Canada, *J. Petrol.,* doi:10.1093/petrology/cgi097.

Herrin, E. & Goforth, T., 1977. Phase-matched filters: application to the study of Rayleigh waves, *Bull. seism. Soc. Am.,* **67,** 1259–1275.

Herrmann, R.B. & Ammon, C.J., 2004. *Computer programs in seismology: Surface waves, receiver functions and crustal structure*, v. 3.30. Saint Louis University, Missouri.

Hwang, H.J. & Mitchell, B.J., 1986. Interstation surface wave analysis by frequency-domain Wiener deconvolution and modal isolation, *Bull. seism. Soc. Am.,* **76,** 847–864.

Kopylova, M.G. & Caro, G., 2004. Mantle xenoliths from the southeastern Slave craton: evidence for chemical zonation in a thick, cold lithosphere, *J. Petrol.,* **45,** 1045–1067.

Kopylova, M.G., Lo, J. & Christensen, N.I., 2004. Petrological constraints on seismic properties of the Slave upper mantle (Northern Canada), *Lithos,* **77,** 493–510.

Lander, A.V. & Levshin, A.L., 1989. Recording, identification, and measurement of surface wave parameters, in *Seismic Surface Waves in Laterally Inhomogeneous Earth*, pp. 131–182, ed. Keilis-Borok, V.I., Kluwer Academic Publishers, Dordrecht.

Li, A., Forsyth, D.W. & Fischer, K.M., 2003. Shear velocity structure and azimuthal anisotropy beneath eastern North America from Rayleigh wave inversion, *J. geophys. Res.,* **108**(B8), 2362, doi:10.1029/2002JB002259.

Martin, B.E. & Thomson, C.J., 1997. Modelling surface waves in anisotropic structures, II: Examples, *Phys. Earth planet. Inter.,* **103,** 195–206.

Menke, W. & Levin, V., 2003. The cross-convolution method for interpreting SKS splitting observations, with application to one and two-layer anisotropic earth models, *Geophys. J. Int.,* **154,** 379–392.

Montagner, J-P., Griot-Pommera, D-A. & Lavée, J., 2000. How to relate body wave and surface wave anisotropy? *J. geophys. Res.,* **105,** 19 015–19 027.

Özalaybey, S. & Savage, M.K., 1994. Double-layer anisotropy resolved from S phases, *Geophys. J. Int.,* **117,** 653–664.

Pedersen, H.A., Coutant, O., Deshamps, A., Soulage, M. & Cotte, N., 2003. Measuring surface wave phase velocities beneath small broad-band arrays: test of an improved algorithm and application to the French Alps, *Geophys. J. Int.,* **154,** 903–912.

Pedersen, H.A., Bruneton, M., Maupin, V. & the Svekalapko seismic tomography working group, 2006. Lithospheric and sublithospheric anisotropy beneath the Baltic Shield from surface wave array analysis, *Earth planet. Sci. Lett.,* **244,** 590–605.

Rümpker, G. & Silver, P.G., 1998. Apparent shear-wave splitting parameters in the presence of vertically varying anisotropy, *Geophys. J. Int.,* **135,** 790–800.

Rümpker, G., Tommasi, A. & Kendall, J.-M., 1999. Numerical simulations of depth-dependent anisotropy and frequency-dependent wave propagation effects, *J. geophys. Res.,* **104,** 23 141–23 153.

Saltzer, R.L., Gaherty, J.B. & Jordan, T.H., 2000. How are vertical shear wave splitting measurements affected by variations in the orientation of azimuthal anisotropy with depth?, *Geophys. J. Int.,* **141,** 374–390.

Savage, M.K., 1999. Seismic anisotropy and mantle deformation: what have we learned from shear wave splitting?, *Rev. Geophys.,* **37,** 65–106.

Schultze-Pelkum, V. & Blackman, D.K., 2003. A synthesis of seismic P and S anisotropy, *Geophys. J. Int.,* **154,** 166–178.

Silver, P.G. & Chan, W.W., 1991. Shear wave splitting and subcontinental mantle deformation, *J. geophys. Res.,* **96,** 16 429–16 454.

Silver, P.G. & Savage, M.K., 1994. The interpretation of shear wave splitting parameters in the presence of two anisotropic layers, *Geophys. J. Int.,* **119,** 949–963.

Snyder, D.B. & Lockhart, G.D., 2005. Kimberlite trends in NW Canada, *J. Geol. Soc. Lond.,* **162,** 737–740.

Snyder, D.B., Bostock, M.G. & Lockhart, G.D., 2003. Two anisotropic layers in the Slave craton, *Lithos,* **71,** 529–539.

Snyder, D.B., Rondenay, S., Bostock, M.G. & Lockhart, G.D., 2004. Mapping the mantle lithosphere for diamond potential using teleseismic methods, *Lithos,* **77,** 859–872.

Thomson, C.J., 1997. Modelling surface waves in anisotropic structures, I: Theory, *Phys. Earth planet. Inter.,* **103,** 195–206.

Vinnik, L.P., Makayeva, L.I., Milev, A. & Usenko, A.Y., 1992. Global patterns of azimuthal anisotropy and deformations in the continental mantle, *Geophys. J. Int.,* **111,** 433–447.

Wiener, N., 1949. *Time-Series*, M.I.T. Press, Cambridge, Massachusetts, 163 pp.